

## Rotational energy surfaces and highJ eigenvalue structure of polyatomic molecules

William G. Harter and Chris W. Patterson

Citation: *The Journal of Chemical Physics* **80**, 4241 (1984); doi: 10.1063/1.447255

View online: <http://dx.doi.org/10.1063/1.447255>

View Table of Contents: <http://scitation.aip.org/content/aip/journal/jcp/80/9?ver=pdfcov>

Published by the [AIP Publishing](#)

---

### Articles you may be interested in

[Multiperturbation approach to potential energy surfaces for polyatomic molecules](#)

*J. Chem. Phys.* **102**, 4919 (1995); 10.1063/1.469540

[Reply to "Comment on 'Rotational energy surfaces and highJ eigenvalue structure of polyatomic molecules'"](#)

*J. Chem. Phys.* **84**, 5218 (1986); 10.1063/1.450644

[Comment on "Rotational energy surfaces and highJ eigenvalue structure of polyatomic molecules"](#)

*J. Chem. Phys.* **84**, 5216 (1986); 10.1063/1.450643

[Erratum: Rotational energy surfaces and highJ eigenvalue structure of polyatomic molecules \[\*J. Chem. Phys.\* \*\*80\*\*, 4255 \(1984\)\]](#)

*J. Chem. Phys.* **81**, 6412 (1984); 10.1063/1.447308

[The Calculation of Perturbation Energies in Vibrating Rotating Polyatomic Molecules](#)

*J. Chem. Phys.* **16**, 453 (1948); 10.1063/1.1746918

---



# Rotational energy surfaces and high- $J$ eigenvalue structure of polyatomic molecules

William G. Harter<sup>a)</sup>

School of Physics, Georgia Institute of Technology, Atlanta, Georgia 30332

Chris W. Patterson

Theoretical Division, Los Alamos National Laboratory, Los Alamos, New Mexico 87545

(Received 20 November 1983; accepted 2 February 1984)

A rotational analog of the vibrational potential energy surface is introduced for describing the rotational fine structure of polyatomic molecules. Classical trajectories on rotational energy (RE) surfaces are related to quantum rotational eigenvalue structure. Interpretation of RE surfaces shows how very different types of molecules may undergo dynamical symmetry breaking and a corresponding clustering of rotational energy sublevels for high angular momentum ( $J > 10$ ). Cluster splitting and spacing are calculated using semiclassical quantization methods. Some consequences of dynamical symmetry breaking such as mixing of nuclear spin species are discussed qualitatively.

## I. INTRODUCTION

The detailed understanding of gas phase photochemistry and molecular dynamics should include a knowledge of the rotational behavior of polyatomic molecules. However, many polyatomic molecules tend to populate rotational states with fairly high angular momentum ( $J \geq 10$ ); and for each  $J$  one expects, in general, to have a complex fine structure of rovibronic sublevels. Therefore, it is not surprising that the rotational dynamics of many polyatomic molecules are often treated only approximately or not at all.

Since the discovery of infrared multiple-photon dissociation of polyatomic molecules, there have been a significant number of detailed infrared absorption studies of vibrational fundamentals and overtones of  $\text{SF}_6$ ,<sup>1-11</sup>  $\text{SiF}_4$ ,<sup>12-15</sup>  $\text{CF}_4$ ,<sup>16,17</sup>  $\text{UF}_6$ ,<sup>18</sup> and similar "heavy" spherical top molecules. These studies required a very detailed knowledge of the rovibrational fine structure. Some surprising results of all these studies are experimental observations of spectral clustering effects. The high- $J$  fine structure turns out to be much simpler than expected because most of the rovibrational sublevels are "clustered" together into nearly degenerate multiplets.<sup>19</sup> There is a simple *fine* structure splitting between the clustered sublevels and a *superfine* structure splitting within the clusters themselves. This superfine splitting is often unresolved. The comparative simplicity of the clustered spectra leads to a relatively simple theory of dynamical or "spontaneous" symmetry breaking which explains the form of superfine structure within the spectral clusters.<sup>20-24</sup>

Although dynamical symmetry breaking of rotational states was first noticed in spherical top molecules, it can happen even more readily (i.e., for lower angular momentum) in molecules with less symmetry such as asymmetric top molecules. One objective of this article will be to show the generality of the clustering phenomenon by comparing these two different types of rotors. Indeed, we expect that the

spectra of heavy asymmetric top molecules, for which very high angular momentum states are populated, will be greatly simplified by dynamical symmetry breaking effects. Furthermore, these effects should allow one to predict and understand rotational superfine structure of high- $J$  levels in virtually all polyatomic molecules.

To understand the consequences of dynamical symmetry breaking in polyatomic molecules, we shall introduce in Sec. II the molecular rotational energy (RE) surface in analogy to the general anharmonic vibrational potential energy (PE) surface. The RE surface allows one to picture the classical motion or trajectories of a rotating angular momentum vector  $J$  in the body frame. Such a picture enables one to analyze quantum rotational dynamics and spectra.

We shall show in Sec. III that it is a simple matter, using the RE surface, to classically interpret the quantum fine and superfine structure. In Sec. IV, we show that this structure is easily calculated semiclassically. The fine structure splitting is calculated by quantizing the action for trajectories on the RE surface while the superfine cluster splitting is calculated from the tunneling integrals between equivalent classical trajectories. Since the tunneling involves purely kinetic terms in the Hamiltonian, it is a *dynamical* tunneling between trajectories about equivalent rotational axes in the body frame. For high- $J$ , this tunneling is much easier to calculate semiclassically than quantum mechanically.

The semiclassical quantization on the RE surface makes use of the work of Colwell, Handy, and Miller,<sup>25</sup> as well as earlier quantization schemes of King *et al.*<sup>26,27</sup> and Born.<sup>28</sup> Although the emphasis of Colwell *et al.* was for low- $J$  spectra of asymmetric top molecules, their methods are more accurate for high- $J$  clusters in rigid asymmetric top spectra. We extend their usefulness here to deformable or semirigid molecules having arbitrary equilibrium structure or symmetry. This includes spectra of semirigid spherical top molecules.

The symmetry labeling of clusters is discussed in Sec. V. The cluster labeling scheme depends on the symmetry breaking subgroup and its induced representations in the full group of the RE surface. We give examples of this math-

<sup>a)</sup> Presently on leave at the Theoretical Division, Los Alamos National Laboratory, Los Alamos, NM 87545.

emational structure as applied to asymmetric and spherical top molecules.

There are some unexpected properties and effects associated with dynamical symmetry breaking and superfine structure. As discussed in Sec. VI, one finds quantum rotational levels belonging to different nuclear spin symmetry species (e.g., *ortho* and *para* species) within each superfine multiplet or cluster. Many clusters have superfine splittings between sublevels of less than a kilohertz in frequency. It is known that nuclear magnetic hyperfine splittings in many polyatomic molecules are usually several kilohertz or more. (Electric quadrupole splittings can be much more.) The presence of small superfine splitting allows for the strong resonant mixing of different nuclear spin species. Thus, for many polyatomic molecules in high angular momentum states, the normally "forbidden" interspecies transitions can easily occur.

Until recently, it was thought that such interspecies transitions would not occur. In fact, Herzberg has summarized the prevailing opinion by stating the following selection rules.<sup>29</sup>

*"As previously, transitions between rotational levels of different (overall) species are very strictly forbidden, since the coupling of the nuclear spin with the rest of the molecule is so extremely weak... These selection rules hold even for collisions, and therefore any particular gas consists of as many almost nonconvertible modifications as there are rotational species of its molecules."*

However, the generally accepted rules do not account for the almost unavoidable mixing of nuclear spin species due to dynamical symmetry breaking for high  $J$ . With the basic understanding of superfine structure there came predictions<sup>24,30</sup> of widespread and strong nuclear spin species mixing. The first spectroscopic evidence of such mixing was found by the Bordés and co-workers in SF<sub>6</sub> saturation absorption spectroscopy.<sup>31,32</sup>

Very high resolution spectroscopic techniques such as those applied by Ch. Bordé to SF<sub>6</sub> should soon be used in studies of a wide range of other polyatomic molecules. One objective of this article is to provide methods that may aid in the planning and interpretation of such detailed studies of molecular spectra. We provide methods for predicting and calculating fine and superfine rotational structure and its associated effects for polyatomic molecules in general. We shall describe a theory of dynamical symmetry breaking in which a rigid asymmetric top molecule can be treated on the same footing with a semirigid octahedral spherical top molecule for which the spectral clustering is well known. There are then many examples of semirigid polyatomic molecules whose symmetry fall somewhere in between those treated here. However, our examples of asymmetric and octahedral rotors should be sufficient to illustrate general methods and salient features of dynamical symmetry breaking.

## II. MOLECULAR DYNAMICS ON ROTATIONAL ENERGY (RE) SURFACES

For understanding rotational fine structure of polyatomic molecules, it is helpful to introduce the concept of rotational energy (RE) surfaces. The RE surfaces can be as useful

for elucidating rotational sublevels and transitions as the molecular potential energy (PE) surfaces are for describing vibrational levels and their spectral structure. Comparisons between RE surfaces and more commonly known PE surfaces are made in Sec. II A.

Examples of known RE surfaces are shown in Figs. 1 and 2. The two examples in Fig. 1 represent surfaces for a rigid symmetric and asymmetric top molecule, and the third example in Fig. 2 represents an octahedrally symmetric semirigid spherical top molecule. These RE surfaces are explained qualitatively in Sec. II A and quantitatively in Sec. II B in terms of classical mechanics and Hamilton's equations. In Fig. 3 is shown a sketch of a more general RE surface which is discussed briefly at the end of Sec. II B.

### A. Qualitative features of RE surfaces

Since the early work of Born and Oppenheimer, the effective potential energy (PE) surface has been a key concept in molecular dynamics. The PE surface is supposed to represent the adiabatic energetics of a single energy-isolated electronic quantum state or level. The nuclear vibrational frequencies are supposed to be low enough that the electronic wave undergoes adiabatic response to vibration. Generally, this means that the relevant vibrational spectra have much lower frequencies than those of the lowest electronic resonances, i.e., the nuclei are much slower than the electrons.

Generally, the PE surfaces for  $N$  nuclei occupy a  $3N-6$ -dimensional coordinate space. The six dimensions which are subtracted from the PE description represent translations and rotations. Our objective is to provide the three rotational degrees of freedom with effective adiabatic energy surfaces of their own which we call the RE surfaces. This will be possible whenever the rotational frequencies are much less than the lowest electronic or vibrational frequencies, i.e., when the rotational motion is much slower than vibrational or electronic motion.

By analogy, one could expect an RE surface to represent the adiabatic energetics of a single energy-isolated vibronic (electronic and vibrational) quantum level. For a freely rotating molecule the total angular momentum  $J$  is a good quantum number as well. In the classical picture of rotation, there exists a laboratory fixed angular momentum vector  $\mathbf{J}$  about which the molecular body may precess and nutate. The RE surface serves to track the motion of  $\mathbf{J}$  in the molecular body frame using a form of spherical polar coordinates described below. Each point on the RE surface represents a direction  $\hat{J}$  of the angular momentum  $\mathbf{J}$  vector in the body frame. As the body rotates in the lab frame, the  $\mathbf{J}$  vector moves from point to point on the RE surface in the body frame. At each point, the radial height of the RE surface is defined to be the adiabatic rotational energy (in arbitrary units), subject to the constraint that the magnitude  $|\mathbf{J}|$  of angular momentum is constant.

The adiabaticity conditions for validity of an RE surface are analogous to the Born–Oppenheimer conditions for a PE surface. However, it is an electronic and vibrational (vibronic) wave function that must respond adiabatically to the rotational motion on a given RE surface. Each RE surface belongs to a given set of electronic, vibrational, and total

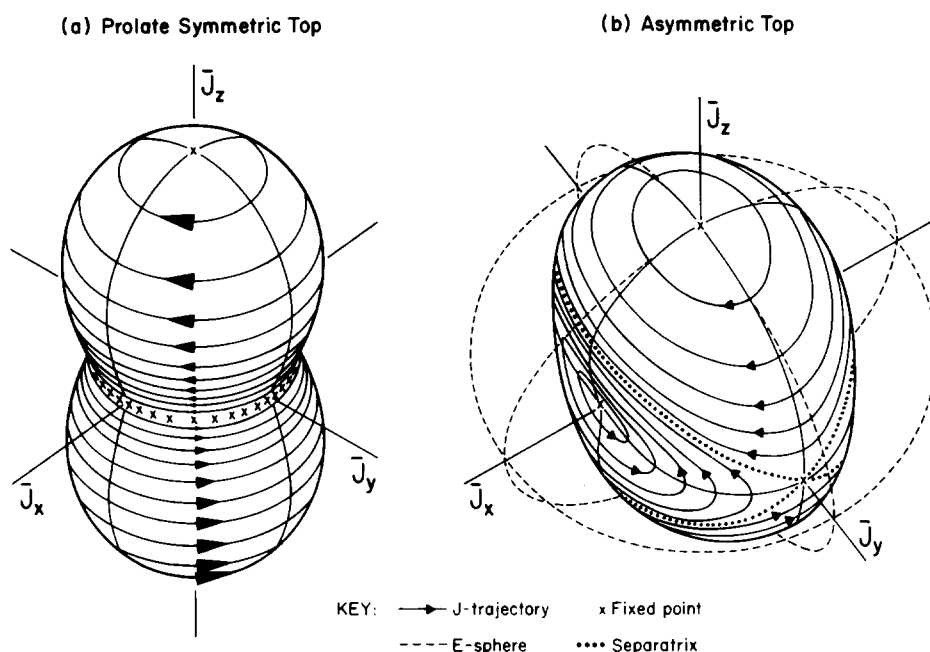


FIG. 1. Rotational energy surfaces for two types of molecules. (a) Rigid prolate symmetric top RE surface. Contour lines correspond to angular momentum trajectories as described in Sec. II. (b) Rigid asymmetric top RE surface. Dotted lines represent the separatrix curves which separate different types of trajectories. Dashed lines correspond to meridians of spherical energy surfaces which intersect the highest energy trajectories. The  $\bar{y}\bar{z}$  meridian is a tunneling path described in Sec. IV.

angular momentum quantum labels  $\epsilon$ ,  $\nu$ , and  $J$ , respectively. This means that all of the centrifugal or Coriolis distortions of the molecule must respond in phase, and keep up with the precessing rotational axis and associated  $\mathbf{J}$  vector. Resonance between rotational and vibronic motion must be negligible. The energy difference between a given RE surface labeled by  $(\epsilon, \nu, J)$  and other  $(\epsilon', \nu', J)$  surfaces must be comparatively large in order to avoid resonances.

In order to understand the meaning of RE surfaces, it is helpful to develop their classical description in analogy to the classical description of PE surfaces. In particular, it is important to see how classical trajectories arise.

For PE surfaces, the trajectories are bounded by a locus of classical turning points which are defined by the intersec-

tion of the PE surface and the constant energy surface. A trajectory starting at such a point would initially move away from the constant- $E$  line and "down" the PE surface. Always the momentum time derivative ( $\dot{\mathbf{p}}$ ) points down the fall line ( $-\dot{\mathbf{p}}$  equals the PE surface gradient), but the subsequent motion of the trajectory depends on the speed and shape of the surface.

The analogous trajectory on the RE surface is comparatively simple since the rotational energy is entirely kinetic. The trajectory of the  $\hat{J}$  unit vector must lie along the intersection of the RE surface and the constant energy sphere. (Recall that energy is plotted radially and so the constant energy surface is spherical.) In other words, classical  $\mathbf{J}$  trajectories are simply the contour lines as shown on the sample RE surfaces in Figs. 1 and 2. The direction of the  $\mathbf{J}$  vector is constrained to follow the contour line, i.e., it moves in a direction that is perpendicular to the fall line at each point on the RE surface. By considering Hamilton's equations, we will show that the speed of  $\mathbf{J}$  is proportional to the slope of the RE surface in partial analogy to PE trajectories.

Note that a RE surface is different from a constant energy (CE) surface. For some purposes, it is desirable to simply plot a CE surface in  $\mathbf{J}$  space. For the rigid symmetric or asymmetric top, the CE surface is the angular momentum ellipsoid.<sup>33,34</sup> This, in turn, can be related by tangent plane construction to the angular velocity ellipsoid which is the geometrical description used in most texts on rigid rotational dynamics.<sup>34</sup> The intersection of a CE surface with constant  $J$  concentric spheres also produces possible  $\mathbf{J}$ -vector trajectories in a way that is similar to the RE surface construction. The difference is that CE surfaces have the same energy but varying  $J = |\mathbf{J}|$ , while RE surfaces have the same  $J$  but different energy. For molecular fine structure spectroscopy the RE surfaces provide a more convenient format for displaying the motion of  $\mathbf{J}$  vectors.

Before considering the details of rotational coordinates

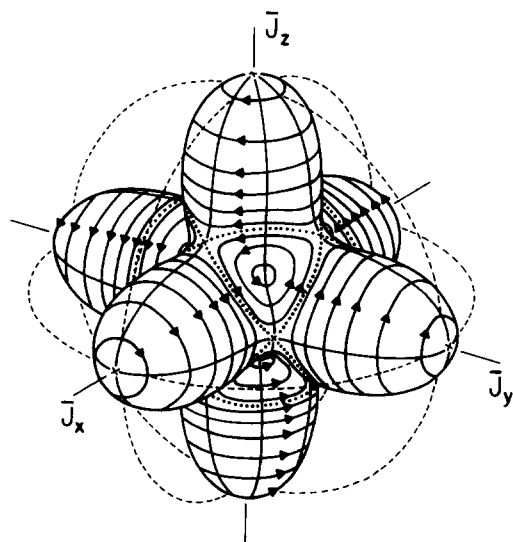


FIG. 2. Rotational energy surface for semirigid octahedral spherical top molecule. Dotted lines indicated separatrices and dashed lines indicate tunneling paths for highest energy trajectories.

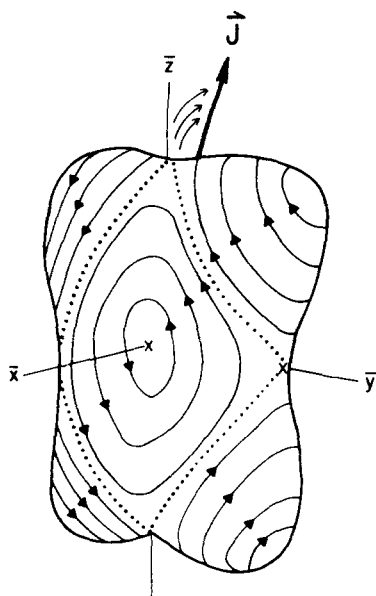
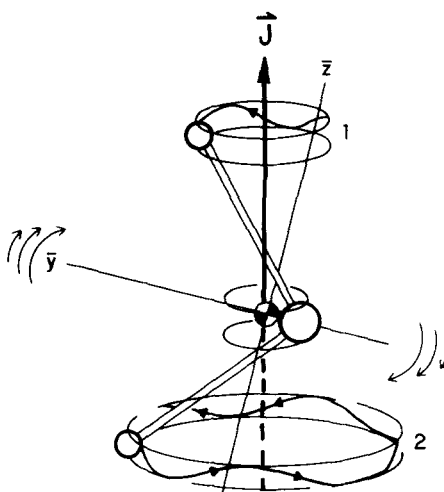
(a) Body Frame View ( $\mathbf{J}$  moving)(b) Lab Frame View ( $\mathbf{J}$  fixed)

FIG. 3. Rotational energy surface and associated rotational dynamics for a hypothetical semi-rigid asymmetric molecule. (a) RE surface and trajectories are sketched in body frame. (b) Rotational motion of an  $XY_2$  molecule associated with one corner trajectory is sketched in the laboratory frame.

and momenta, it is perhaps useful to mention some further qualitative properties of RE surfaces. RE surfaces often have a shape that is at least roughly similar to that of the molecule which they represent. For example, Fig. 1(a) represents a rigid prolate symmetric top molecule whose long axis (and axis of minimum inertia) is the  $\bar{z}$  axis, while the  $\bar{x}$  and  $\bar{y}$  axes have larger but equal inertia. As another example, Fig. 1(b) represents a rigid asymmetric top molecule whose longest and shortest body axes are  $\bar{z}$  and  $\bar{x}$ , respectively. A planar ethylene-like  $X_2-Y=Y-X_2$  molecule might have a RE surface something like Fig. 1(b) or Fig. 3(a) with the  $\bar{z}$  axis along the  $Y=Y$  bond and the  $\bar{x}$  axis normal to the molecular plane. In Fig. 1(b) the highest energies, and hence the lowest effective inertia, occur for rotations about the  $\bar{z}$  axis.

As a third example, Fig. 2 represents an octahedral  $XY_6$  spherical top molecule such as  $SF_6$ . If  $SF_6$  were truly a rigid spherical top, then its RE surface would just be a sphere, and its spectral and dynamics might be much less interesting. Instead, the  $SF_6$  molecule is held together by radial S-F bonds that are much stronger than the angular F-F "bonds." Consequently, when the  $\mathbf{J}$  vector is located near a threefold symmetric (1,1,1) axis, the molecule is more distorted by centrifugal forces than when rotating (with the same  $|\mathbf{J}|$ ) around a fourfold symmetric (1,0,0) axis. This is indicated clearly by the presence of eight threefold symmetric valleys and six fourfold symmetric hills on the RE surface in Fig. 2.

It should be pointed out that molecular rotations in the opposite direction but with the same magnitude  $|\mathbf{J}|$  should have the same energy. This amounts to requiring that the Hamiltonian be invariant to time reversal or momentum inversion ( $\mathbf{J} \rightarrow -\mathbf{J}$ ), and that a RE surface have inversion symmetry even if the actual molecule which it represents does not. Therefore, Fig. 1(b) can also represent an asymmetric top molecule of the bent  $XYX$  form with the  $\bar{x}$  axis normal to

the  $XYX$  plane and the  $y$  axis passing through  $Y$ . [In fact, the constants embodied in Fig. 1(b) are fairly close to those of  $H_2O$ .] Similarly, Fig. 2 can also represent a tetrahedral  $XY_4$  molecule.

## B. Quantitative analysis of RE surfaces for rigid and semirigid molecules

The RE surfaces provide ways to visualize the dynamical properties associated with model rotor Hamiltonians. Trajectories on the RE surfaces have to lie on curves corresponding to the intersection of the RE surface with a constant energy sphere as described previously. However, to understand the detailed time behavior on these trajectories requires solving Hamilton's equations as described in this section. Classical solutions of Hamilton's equations involving rigid and semirigid polyatomic molecules will be discussed.

### 1. Rigid symmetric and asymmetric top molecules

The RE surfaces drawn in Figs. 1(a) and 1(b) are derived from a Hamiltonian of the form

$$H = AJ_{\bar{x}}^2 + BJ_{\bar{y}}^2 + CJ_{\bar{z}}^2, \quad (2.1)$$

where  $A$ ,  $B$ , and  $C$  are molecular constants which are inversely proportional to the rotational inertia on the  $\bar{x}$ ,  $\bar{y}$ , and  $\bar{z}$  axes, respectively. Figure 1(a) represents a prolate symmetric top molecule in which  $A = B < C$ . Figure 1(b) represents a most-asymmetric top molecule where  $B$  is half-way between  $A$  and  $C$ .

As previously mentioned, the RE surface is a radial plot of the energy as a function of the direction of the vector  $(J_{\bar{x}}, J_{\bar{y}}, J_{\bar{z}})$  in the body frame subject to the constraint

$$J^2 = J_{\bar{x}}^2 + J_{\bar{y}}^2 + J_{\bar{z}}^2 = \text{const.} \quad (2.2)$$

This direction is in terms of body polar coordinates  $(\gamma, \beta)$  as defined in Appendix A. A convenient way to plot this is to

first rewrite the Hamiltonian in terms of angular momentum spherical harmonics  $Y_k^J(\gamma, \beta)$  or unit multipole functions  $C_k^J(\gamma, \beta)$ , where

$$C_k^J = (4\pi/2J + 1)^{1/2} Y_k^J. \quad (2.3)$$

These provide one with explicit and well known functions of the Euler angles. For example, using the  $J = 2$  or quadrupole functions we have

$$\begin{aligned} C_0^2 &= (3 \cos^2 \beta - 1)/2 = (-J_{\bar{x}}^2 - J_{\bar{y}}^2 + 2J_{\bar{z}}^2)/(2J^2), \\ (C_2^+ + C_{-2}^-) &= (\sin^2 \beta \cos 2\gamma)(3/2)^{1/2} \\ &= (J_{\bar{x}}^2 - J_{\bar{y}}^2)(3/2)^{1/2}/J^2. \end{aligned}$$

One may then rewrite the general rigid rotor Hamiltonian as follows:

$$\begin{aligned} H &= J^2[(A + B + C)/3] + J^2[(2C - A - B)/3]C_0^2 \\ &\quad + J^2[(A - B)/\sqrt{6}](C_2^+ + C_{-2}^-). \end{aligned} \quad (2.4)$$

The first term in Eq. (2.4) is the only nonzero term for a rigid spherical top molecule in which  $A = B = C$ . Only the first and second terms survive for a rigid symmetric top molecule in which  $A = B \neq C$  and the resulting RE surface is shown in Fig. 1(a). Finally, the third term adds the asymmetry to give the rigid most-asymmetric top [ $B = (A + C)/2$ ] RE surface shown in Fig. 1(b).

In Fig. 1 we have plotted the constant energy contour lines for the symmetric and most-asymmetric top molecules using Eq. (2.4). The  $\mathbf{J}$  vector must follow paths on these contour lines. Indeed, for the symmetric top molecule, the  $\mathbf{J}$  vector precesses around the circles on the RE surface shown in Fig. 1(a). It is instructive to obtain the same results using Hamilton's equations. Using the Hamiltonian Eq. (2.1) with  $A = B \neq C$ , we may rewrite it in terms of Euler angles and the conjugate Euler momenta as described in Appendix A [see Eq. (A11)]. We have

$$H = B [(J_\alpha - J_\gamma \cos \beta)^2 / (\sin^2 \beta) + J_\beta^2] + CJ_\gamma^2. \quad (2.5)$$

Hamilton's equations then give

$$\dot{\alpha} = \frac{\partial H}{\partial J_\alpha} = 2B (J_\alpha - J_\gamma \cos \beta) / (\sin^2 \beta), \quad (2.6a)$$

$$\dot{\beta} = \frac{\partial H}{\partial J_\beta} = 2BJ_\beta, \quad (2.6b)$$

$$\begin{aligned} \dot{\gamma} &= \frac{\partial H}{\partial J_\gamma} \\ &= -2B (J_\alpha - J_\gamma \cos \beta) \cos \beta / (\sin^2 \beta) \\ &\quad + 2CJ_\gamma. \end{aligned} \quad (2.6c)$$

We have shown in Appendix A that the RE contour lines define the loci of the lab axis in the body frame if the  $\mathbf{J}$  vector is defined to be along the lab  $z$  axis. This is equivalent to demanding the following [using Eqs. (A10)–(A11)]:

$$J_\alpha = J_z \equiv J, \quad J_\beta = 0, \quad J_\gamma = J_{\bar{z}} = J \cos \beta. \quad (2.7)$$

This reduces the equations of motion above to the following:

$$\dot{\alpha} = 2BJ, \quad (2.8a)$$

$$\dot{\beta} = 0, \quad (2.8b)$$

$$\dot{\gamma} = 2(C - B)J \cos \beta. \quad (2.8c)$$

This verifies that the  $\mathbf{J}$  vector does indeed trace a circular (i.e.,  $\dot{\beta} = 0$ ) cone in the body frame. For a prolate ( $C > B$ ) top such as is represented by Fig. 1(a), the precession is *clockwise* since Eq. (2.8c) implies  $\dot{\gamma} > 0$ , but the *body* azimuth angle sense is reversed ( $-\gamma$ ) as described in Appendix A. It is important to notice that the precessional frequency vanishes for  $\mathbf{J}$  vectors on the equator ( $\beta = \pi/2$ ) of a symmetric top. The equator is a line of fixed points indicated by (xxx) in Fig. 1(a). The poles are fixed points, as well.

An equatorial line of fixed points is the only part of the RE surface which remains for a diatomic rotor or a linear rotor in a  $\Sigma$  vibronic state. Any part of a linear rotor RE surface involving nonzero  $J_z$  component must approach infinity as the  $\bar{z}$  moment of inertia vanishes or  $C \rightarrow \infty$  [see Eq. (2.1)]. The elementary RE surface is meant to describe internal angular momentum trajectories and dynamics of nonlinear *polyatomic* molecules. The classical  $\mathbf{J}$  vector for a diatomic molecule must always be fixed in the body frame as well as in the lab frame.

In general, the speed and direction with which a  $\mathbf{J}$  vector moves along a given trajectory is determined by the slope or gradient of the energy surface at each point. This is expressed by Hamilton's equation for the angular velocity vector  $\omega$ ,

$$\omega_i = \frac{\partial H}{\partial J_i} \quad \text{for } i = \bar{x}, \bar{y}, \bar{z} \quad (2.9a)$$

or

$$\omega = \nabla_J H. \quad (2.9b)$$

For a constant energy (CE) surface,  $\omega$  is normal to the tangent plane at each point. For RE surfaces this leads to the following left-handed mnemonic: trajectories circulate clockwise around high points and counterclockwise around low points.

The asymmetric top RE surface shown in Fig. 1(b) has a high around the  $\bar{z}$  axis and a low around the  $\bar{x}$  axis. The sense of precession is clockwise around the  $\bar{x}$  axis and counterclockwise around the  $\bar{z}$  axis as shown in Fig. 1(b). The  $\bar{x}$  and  $\bar{z}$  neighborhoods are delineated by what are called *separatrix* trajectories. These are dotted trajectories which go over the saddle points on the  $\bar{y}$  axis in Fig. 1(b). The saddle points are hyperbolic or unstable fixed points with zero slope but whose curvature is positive or negative depending on the direction in which it is measured. Trajectories in the neighborhood of separatrices are associated with erratic (but not chaotic) motion and nonuniform time behavior.<sup>33,34</sup> An asymmetric top molecule set in motion near a saddle point will spin for awhile and then precipitously flop almost completely over spinning around the opposite axis for awhile until repeating this process.<sup>34</sup> The period for the flopping process approaches infinity as the corresponding trajectory approaches the separatrix. A  $\mathbf{J}$  vector exactly on a separatrix will never pass the next saddle point. It is interesting to note that the separatrices for a rigid asymmetric top are two circles which intersect at the saddle point on the  $\bar{y}$  axis. The angle between each circle and the  $\bar{z}$  axis is  $\theta = \arctan\{(B - C)/(A - B)\}^{1/2}$ .

## 2. Semirigid spherical top molecules

The RE surface drawn in Fig. 2 is derived from a Hamiltonian of the form

$$H = BJ^2 + 10r_{044}(J_x^4 + J_y^4 + J_z^4 - 3J^4/5), \quad (2.10)$$

where, again, the energy is plotted radially for constant  $J = |\mathbf{J}|$ . The anisotropic or tensorial part of the Hamiltonian is the lowest degree nonspherical operator allowed by octahedral symmetry. It may be written in terms of multipole functions Eq. (2.3) as follows:

$$\begin{aligned} & J_x^4 + J_y^4 + J_z^4 \\ &= (2J^4/5)[C_0^4 + (5/14)^{1/2}(C_4^4 + C_{-4}^4)] \\ &+ (3/5)J^4 = J^4(7 \cos^4 \beta - 6 \cos^2 \beta \\ &+ \sin^4 \beta \cos 4\gamma + 3)/4. \end{aligned} \quad (2.11)$$

This form facilitates the plotting of the RE surface shown in Fig. 2.

As explained in the preceding section, the  $\mathbf{J}$  vectors precess in a clockwise sense around high points. For example,  $\mathbf{J}$  could go clockwise around any of the six fourfold symmetric hills on the  $\bar{x}$ ,  $\bar{y}$ , or  $\bar{z}$  axes. The trajectories have an opposite or counterclockwise sense around the eight threefold symmetric valleys on the  $(\pm 1, \pm 1, \pm 1)$  axes. The separatrix curves between the hills and valleys are indicated by dots (...) in Fig. 2. They separate the threefold symmetric trajectories from the fourfold symmetric trajectories, and they intersect at saddle points on the 12 twofold symmetry axes  $(0, \pm 1, \pm 1)$ ,  $(\pm 1, 0, \pm 1)$ , and  $(\pm 1, \pm 1, 0)$ . It can be shown that the separatrices are four intersecting great circles on the energy sphere. The planes of these circles are perpendicular to the threefold symmetry axes.

As in the case of the asymmetric top, a classical  $\mathbf{J}$  vector can never pass through a saddle point even though the separatrix trajectory appears to do so. Also,  $\mathbf{J}$  vectors on trajectories near a separatrix may be delayed for long times while passing through the near zero slope neighborhood of a saddle point. The amount of delay is very sensitive to the initial conditions near a separatrix.

Unlike the rigid asymmetric top, the semirigid  $XY_6$  spherical top does not have a single trajectory which circumnavigates the RE surface. In other words, the classical semirigid  $XY_6$  molecule cannot ever roll completely over in the lab frame. All trajectories are confined to more or less smooth precession and nutation about a single threefold or fourfold symmetry axis. Interaxial or rollover motion in an  $XY_6$  molecule is due to quantum tunneling which will be discussed in Sec. IV.

## 3. Semirigid asymmetric top molecules

It is interesting to speculate on the possibilities of RE surface topography for deformable rotors. The rotational dynamics of molecules in higher  $J$  states require higher order tensor terms in their rotational Hamiltonians. The same may be true for light or floppy molecules, although one must be sure that the deformation follows the rotation adiabatically in order that an accurate theory can be based on isolated RE surfaces for each  $J$  value.

In Fig. 3(a) is sketched an RE surface for an asymmetric

top molecule where higher order tensor terms were included. The result is a new set of contour lines or trajectory orbits located in between the  $\bar{z}$ - and  $\bar{y}$ -symmetry axes. In other words, the RE surface in Fig. 3 has "corners" which were absent in the rigid rotor RE surface seen in Fig. 1(b).

Figure 3(b) contains a sketch in the lab frame of the rotational motion of an  $XY_2$  molecule corresponding to one of the corner trajectories on the hypothetical RE surface in the body frame. A molecule with such an RE surface trajectory would precess around axes that were located at various nonsymmetry points in the body frame.

It is beyond the scope of this work to discuss which RE surfaces are possible in general. The range of possibilities is great and will require a comprehensive study of the algebra and geometry of RE surfaces for higher order tensors appropriate for an asymmetric top molecule. Similar studies are needed for other symmetry types.

## III. DYNAMICAL SYMMETRY BREAKING AND CLASSICAL ROTATIONAL TRAJECTORIES OF POLYATOMIC MOLECULES

In Sec. III below we compare rotational eigenvalue structures with classical trajectories for corresponding energies on RE surfaces. Comparison is also made between eigenvalues and trajectories for the two very dissimilar cases represented by the completely asymmetric rigid rotor RE surface in Fig. 1(b) and the high symmetry semirigid  $XY_6$  rotor RE surface in Fig. 2. Despite their obvious differences, it can be demonstrated that both quantum rotors undergo similar dynamical symmetry breaking effects. The qualitative classical nature of these effects can be described by simple methods given here. The quantitative semiclassical details are also quite simple to derive as explained in the following Sec. IV.

### A. Spectral clusters

By computer one may diagonalize the rotational Hamiltonians for asymmetric and spherical top molecules given by Eqs. (2.1) and (2.10) using the rotor  $|J, k\rangle$  basis where  $k$  is the projection of the angular momentum about any *body* axis. An example of an eigenvalue spectrum is shown for a most-asymmetric rigid rotor with  $J = 10$  in Fig. 4 and for a semirigid spherical rotor with  $J = 30$  in Fig. 5. In both cases the total spectral degeneracy is simply  $2J + 1$ . In the case of an asymmetric top with  $D_2$  symmetry we may label the rotational sublevels by species  $A_1, B_1, A_2,$  and  $B_2$  which are singly degenerate, while in the case of a spherical top with  $O$  symmetry we may label the rotational sublevels by species  $A_1, A_2, E, T_1,$  and  $T_2$ . These  $A, E,$  and  $T$  sublevels are singly, doubly, and triply degenerate, respectively. Remarkably, most of the rotational fine structure in the spectra of Figs. 4 and 5 occur in clustered pairs or triplets of sublevels. The *clusters* of sublevels contain the rotational *superfine* structure. Most superfine structures in Figs. 4 and 5 require a large scale magnification in order to resolve separate rotational sublevels within a cluster. This magnification is provided by the enlargement circles drawn next to the unresolved clusters.

The total degeneracy of each cluster corresponds to the number of distinct classical trajectories with the same energy on equivalent parts of the RE surface. To find the classical trajectories for a given cluster, one simply finds the loci of points with that cluster energy on the RE surface. This correspondence is shown in Figs. 4 and 5. For example, the rightmost ( $B_2A_1$ ) cluster in Fig. 4 corresponds to the two smallest oval trajectories around the asymmetric body  $\bar{z}$  and  $-\bar{z}$  axes, while the rightmost ( $A_2T_2E$ ) cluster in Fig. 5 corresponds to the six smallest circular trajectories around each of the six body  $\pm \bar{x}$ ,  $\pm \bar{y}$ , and  $\pm \bar{z}$  axes. The ( $B_2A_1$ ) cluster has twofold degeneracy while the ( $A_2T_2E$ ) cluster has sixfold degeneracy. Note in Figs. 4 and 5 that the total number of classical trajectories corresponding to discrete quantum energies is  $2J + 1$  as required.

It is possible to pick an arbitrary cluster in Figs. 4 and 5 and immediately form a classical picture of the molecule rotating at that energy. For example, the RE surface orienta-

tion shown on the upper right-hand side of Fig. 5 actually corresponds to the  $\mathbf{J}$  vector following the third highest trajectory around the body  $\bar{z}$  axis corresponding to the ( $ET_1A_1$ ) cluster indicated. Therefore, one could picture the body precessing and spinning counterclockwise around this fixed  $\mathbf{J}$  vector in the laboratory frame in such a way that the  $\mathbf{J}$  vector appear to precess clockwise around that third trajectory in the body frame.

## B. Classical and quantum clusters: Fine and superfine structures

The fine and superfine spectral structure provides an indication of the time scales for  $\mathbf{J}$  motion and delocalization. The frequency of classical  $\mathbf{J}$  precession is roughly proportional to the fine structure spacing between a given cluster and its neighbors. This follows from the relations between the classical precessional period and the action integrals derived in the following section. As will be shown in Sec. IV,

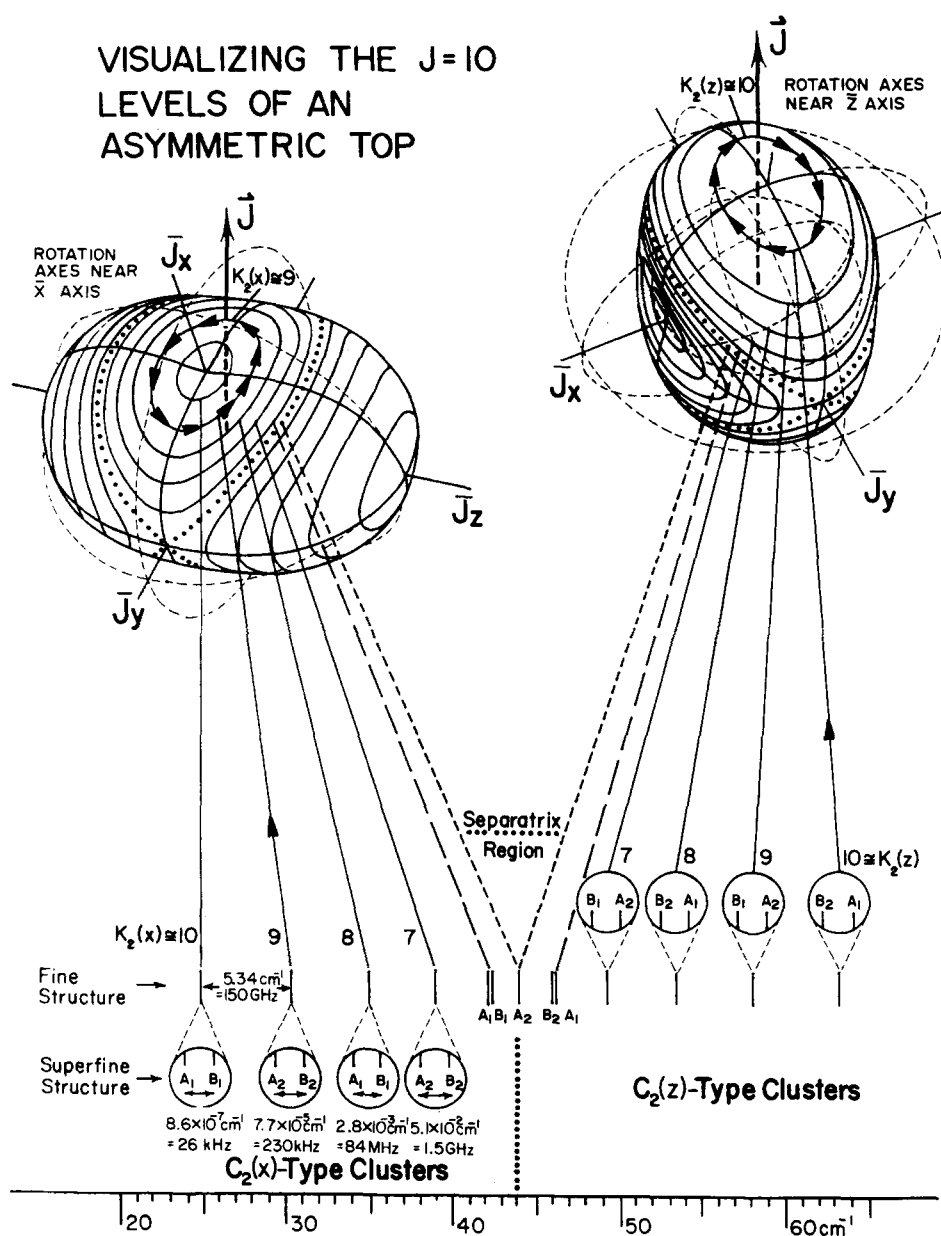


FIG. 4. Rotational spectrum of a most-asymmetric top molecule for  $J=10$  with the corresponding semiclassical trajectories. Rotational constants are for a hypothetical heavy asymmetric top with  $A=0.2$ ,  $B=0.4$ , and  $C=0.6$  (in  $\text{cm}^{-1}$ ).

the energies of the level clusters are derived semiclassically by requiring that the action integrals are multiples of integers, i.e., by the Bohr-Sommerfeld quantization condition

$$A = nh. \quad (3.1)$$

Therefore, the classical frequency  $\nu_c$  is related to the inter-cluster spacing  $\Delta E$ :

$$\nu_c = \frac{\partial E}{\partial A} \simeq \frac{\Delta E}{\Delta n} \frac{\Delta n}{\Delta A} \simeq \Delta E/h. \quad (3.2)$$

On the other hand, the superfine structure or splitting within the cluster is related to the rate at which the  $\vec{J}$  vector delocalizes or tunnels to other equivalent trajectories. As will be shown in Sec. IV, the cluster splittings and tunneling rates are inversely proportional to an exponential of an action path integral across saddle points on the RE surface. Some typical paths are indicated by dashed (---) circles which lie on the energy sphere and connect equivalent trajectories in Figs. 4 and 5. Generally, intracluster splitting decreases exponentially as interconnecting paths become farther from

the saddle points. Hence, the extremal clusters in Figs. 4 and 5 have extremely tiny superfine splittings.

It is easy for superfine splittings to be extremely small at high  $J$ . Equivalently, the times can become very long for tunneling or tumbling between equivalent trajectories on different RE surface hills or valleys. The tunneling time can be so much longer than the times for any other processes in the molecule that it may not be worth considering the tunneling process at all. One can say that the molecule has a reduced symmetry or that it undergoes spontaneous symmetry breaking. One could then regard its wave function as having "collapsed" (in the sense of quantum measurement processes) into a nearly stationary superposition of rotational eigenstates or a mixture of species in which the angular momentum  $\vec{J}$  is localized more like a classical quantity. We shall show in Sec. IV that by calculating the action integrals indicated above, one can semiclassically determine the fine and superfine splittings quite accurately, thus avoiding the quantum mechanical diagonalizations needed for the spectra in Figs. 4 and 5.

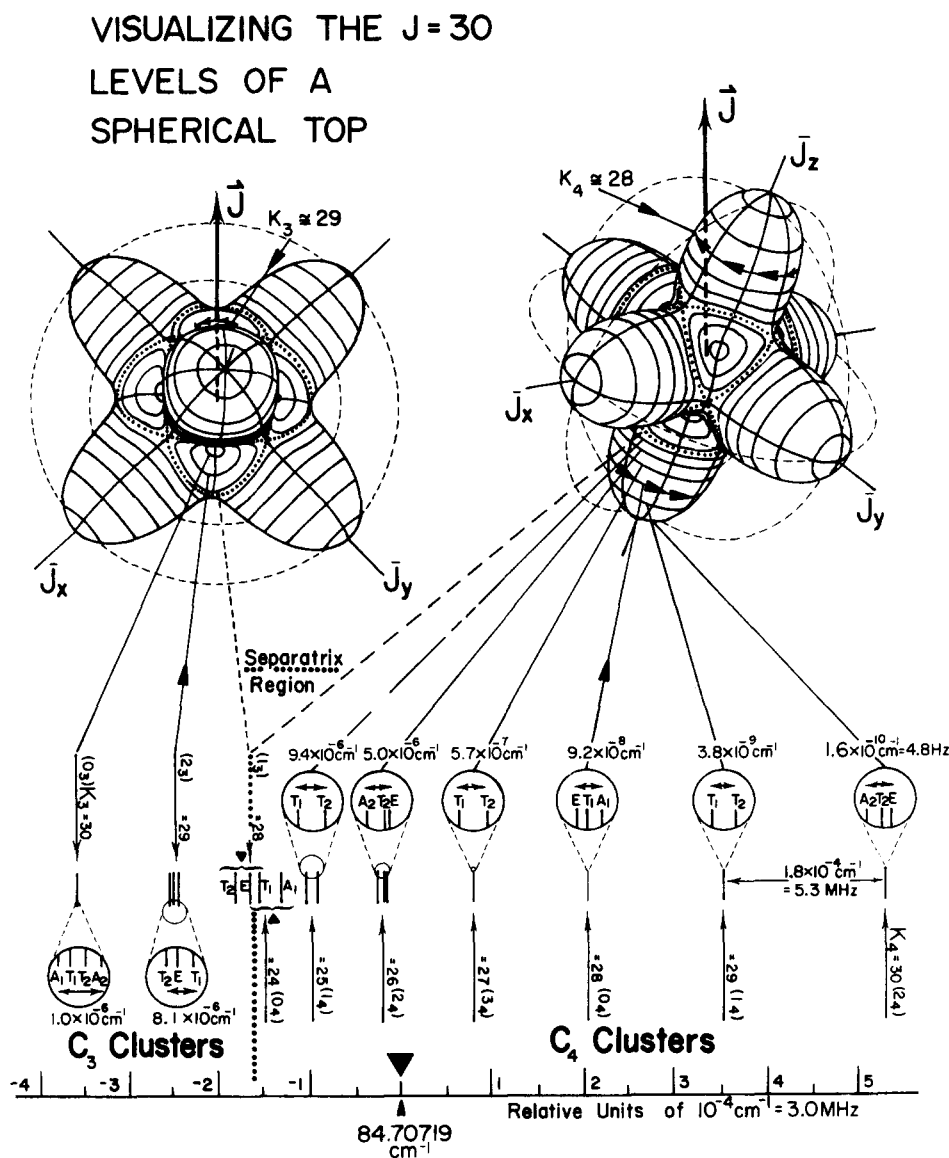


FIG. 5. Rotational spectrum of an octahedral spherical top molecule for  $J = 30$  with the corresponding semiclassical trajectories. Rotational constants are for  $\text{SF}_6$  with  $B = 0.091083 \text{ cm}^{-1}$  and  $t_{044} = 5.44 \text{ Hz}$ . Spectrum is relative to  $BJ(J+1)$ .

Near the separatrices or saddle point regions of Figs. 4 and 5, there is a relatively small spectral region in which the clusters are well broken up. The trajectories near the separatrices are the least localized classical paths with the lowest classical precessional frequency. On the other hand, the quantum tunneling rates are the highest near saddle points since wave functions overlap strongly there. So upon approaching the separatrix energy of the quantum spectrum, one notices a more or less gradual reduction in intercluster or fine structure splitting. But, this is accompanied by an exponential increase in the intracluster or superfine structure splitting due to quantum tunneling or tumbling. The classical motion, quantum eigenvalues, and eigenfunctions are the most complicated, uneven, and difficult to picture in the separatrix region.

The general tendency toward clustering is actually much greater in asymmetric rotor spectra than in the spherical rotors. One sees in Fig. 4 that an angular momentum of only  $J = 10$  is enough to have some asymmetric top cluster whose superfine splittings are less than  $10^{-6}$  times the fine structure splitting. By contrast, for spherical tops one needs angular quanta of  $J = 30$  or higher in order to have comparably small superfine to fine structure ratios (see Fig. 5). The greater tendency for clustering in asymmetric tops is a consequence of the larger angle between equivalent rotational axes. For asymmetric tops this angle is  $180^\circ$  while for spherical tops the angle is  $90^\circ$  and  $55^\circ$  between fourfold axes and between threefold axes respectively. The greater angles correspond to greater barrier integrals and exponentially smaller cluster splittings. As  $J$  increases, the superfine splittings decrease roughly exponentially while the fine structure spacing increases according to a power of  $J$ .

The tendency for asymmetric top spectra to cluster can be clearly shown by varying the asymmetry ratios  $A:B:C$  in the Hamiltonian Eq. (2.1). The asymmetric top levels for  $J = 10$  and  $J = 20$  are plotted in Fig. 6 as a function of  $B$  for fixed  $A = 0.2$  and  $C = 0.6$  (in  $\text{cm}^{-1}$ ). The prolate and oblate symmetric top limits correspond to the left and right hand sides, respectively, of the level correlation diagrams. The separatrix regions in which superfine splittings are comparable to fine structure spacing can be clearly seen along the dia-

gonals of these figures. In the separatrix regions, levels abruptly split from their cluster partner and move up or down in order to switch clusters; and the corresponding eigenfunctions are unusually sensitive to changes in parameters. However, we note again that the classical motion is completely quasiperiodic even in the separatrix region.

The separatrix region for the  $J = 10$  correlation diagram in Fig. 6(a) constitutes a small fraction of the spectrum and it is an even smaller fraction of the  $J = 20$  spectra in Fig. 6(b). In other words, a majority of rotational levels in the thermally accessible range of  $J$  values ( $J = 0-20$  for hydrides and  $J = 0-100$  for "heavy" complexes) are clustered and nearly evenly spaced. Even low- $J$  levels exhibit some clustering, although one might not notice it as easily. In fact, one of the few texts which provides accurate correlation plots (using tables from King *et al.*)<sup>26,27</sup> is Bohr and Mottelson's monograph on *nuclear structure*.<sup>35</sup>

### C. Classical and quantum clusters: Good constants of motion

There is an important difference between the asymmetric rotor model represented in Fig. 4 and the spherical rotor model represented in Fig. 5. This difference concerns the shape of the  $J$ -vector trajectories on the RE surfaces. The trajectories for the octahedral rotor are considerably more planar than those of the asymmetric rotor. Classically, this means that there is considerably more nutation in the asymmetric rotor trajectories. For the spherical rotor, the body projection of angular momentum  $k$  is more likely to be a good constant of the motion. Hence, it is quantitatively useful to label sixfold degenerate clusters in Fig. 5 by  $k_4 = 30, 29, \dots$  and similarly, the eightfold degenerate clusters by  $k_3 = 30, 29, 28$  where  $k_4$  and  $k_3$  are the angular momentum projection about the fourfold and threefold symmetry axes, respectively.

While it is conventional to label asymmetric top levels by  $k_A$  or  $k_C$  quantum numbers, or the angular momentum projection about the  $A$  or  $C$  axes respectively, it is clear from Figs. 4 and 5 that these quantum numbers are not as meaningful as  $k_4$  or  $k_3$ . Since their trajectories are not in a plane, their projections onto their central axes cover a wider range

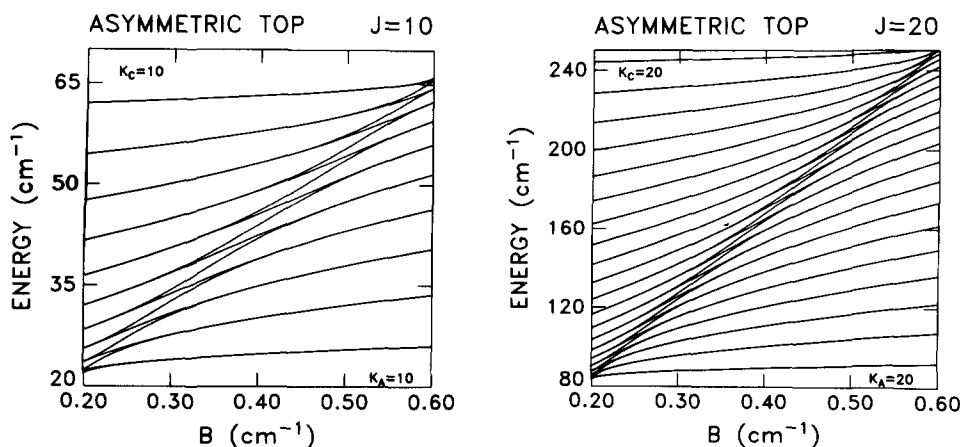


FIG. 6. Level correlations of an asymmetric top molecule for (a)  $J = 10$  and (b)  $J = 20$ . The constants  $A = 0.2 \text{ cm}^{-1}$  and  $C = 0.6 \text{ cm}^{-1}$  are held fixed while  $B$  varies ( $A < B < C$ ). All levels are clustered except along the diagonals of the plots corresponding to the separatrix region on the RE surface.

of  $k$  values and correspond to a large amount of nutational motion. This is consistent with the fact that most asymmetric top eigenvectors contain significant combinations of a correspondingly wide range of  $k$  bases. In contrast, the spherical top eigenvectors are comparatively sharp in  $k$ , and a cluster perturbation theory<sup>36,37</sup> yields accurate approximations for rotational<sup>23</sup> and rovibrational<sup>36-38</sup> eigenvalues. Spherical top molecules behave much like symmetric top molecules with  $k$  a nearly good quantum number about the fourfold and threefold symmetry axes. Thus, the trajectories on the fourfold symmetry axes in Fig. 5 are like the trajectories of the prolate symmetric top in Fig. 1(a) while the trajectories on the threefold symmetry axes in Fig. 5 are like the trajectories of an oblate symmetric top.

It is sometimes convenient to represent states of sharp  $J$  and  $k$  by angular momentum cones of altitude  $k$  and slant length  $\sqrt{J(J+1)}$ . These cones are the loci of the classical angular momentum vector subject to the constraints of the quantum angular momentum eigenvalues of the magnitude  $\langle J^2 \rangle = J(J+1)$  and  $\bar{z}$  component  $\langle J_{\bar{z}} \rangle = k$ . The base of the cone represents the uncertainty of the  $\bar{x}$  and  $\bar{y}$  components of  $\mathbf{J}$ , and the uncertainty is minimum for the substate with the highest  $\bar{z}$  component ( $k = J$ ). The other states belong to wider cones, and the cone's apex angle  $\theta_k$  for arbitrary  $k$  is given by

$$\theta_k = \cos^{-1}[k / (J(J+1))^{1/2}]. \quad (3.3)$$

The angular momentum cones provide an easy way to approximate high- $J$  and high- $k$  fine structure in SF<sub>6</sub> spectra. An example of  $J = 88$  spectra<sup>4</sup> is seen in Fig. 7 to fit rather closely to the intersections of the  $J = 88$  cones<sup>39</sup> and the XY<sub>6</sub> RE surface.<sup>40</sup> Also, one can estimate the  $k$  values for which the three- or fourfold clusters terminate by finding the angles between the three- or fourfold axes and the nearest separatrices. Since the separatrix planes are normal to the threefold axes, a separatrix subtends an angle of  $\cos^{-1} \sqrt{2/3} = 35.3^\circ$  with the nearest fourfold axis and an angle of  $\cos^{-1} \sqrt{1/3} - 35.3^\circ = 19.5^\circ$  with the nearest threefold axis as shown in Fig. 7. These angles determine the cutoff values  $k_4(\text{last}) = 72.3$  and  $k_3(\text{last}) = 83.4$ , corresponding to the largest cones that can fit in the regions around the fourfold and threefold axes defined by the separatrix.

Actually, the cone diagram slightly underestimates the number of clusters for the octahedral spherical rotor. Close examination of the  $P(88)$  spectra reveals one or two "extra" clusters that manage to squeeze in on either side of the separatrix region. This is understandable since they correspond to nonplanar trajectories near the separatrix for which  $k$  is not sharp, and cones are poor approximations of angular momentum loci. In contrast, an asymmetric rotor has many more clusters than predicted by a cone diagram since most of its eigenstates correspond to irregular nonplanar trajectories for which  $k$  is not sharp.

Since asymmetric rotor clusters are all doublets, it is possible they might be confused with the well understood orbital doublets of sharp  $\pm k$  quanta. This point of confusion does not arise in the octahedral clusters since they are sextets and octets which cannot be confused with any normal orbital symmetry degeneracy. Nevertheless, it is useful

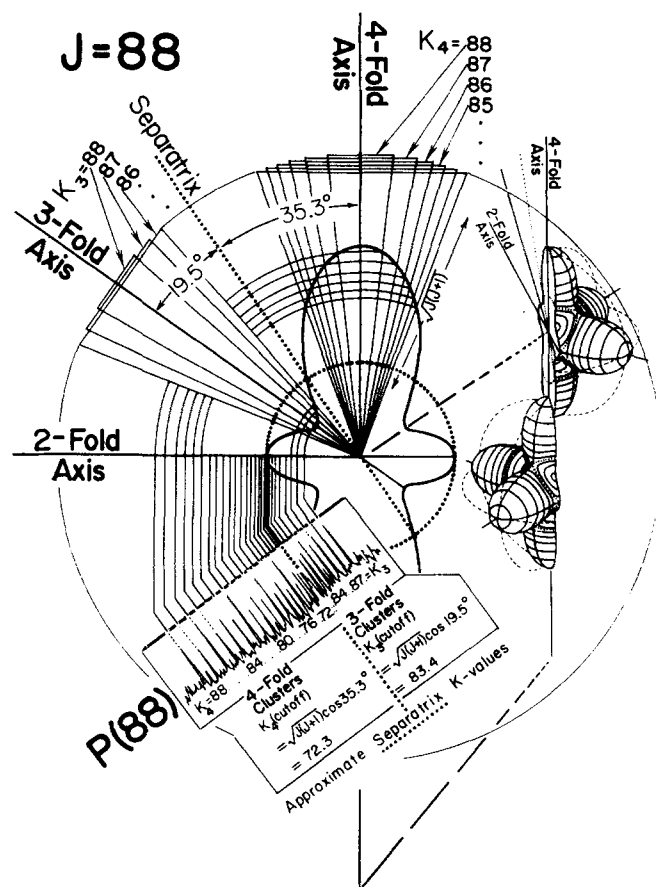


FIG. 7. The fine structure spectrum of  $P(88)$  for  $\nu_4$  of SF<sub>6</sub> is correlated with the intersections of the RE surface and the  $J = 88$  angular momentum cones. A cross section of the RE surface from Fig. 2 is shown which contains the two-, three-, and fourfold symmetry axes. Intersections of the sides of angular momentum cones approximates the energy levels and fine structure clusters in the spectrum (after Kim *et al.* from Ref. 4.) The angle between the separatrix plane and the three- or fourfold axes determines the lowest momentum  $k_3$  or  $k_4$  for the three- or fourfold clusters near the separatrix energy.

to contrast the concept of orbital degeneracy due to symmetry with the notion of cluster degeneracy associated with spontaneous or dynamical symmetry breaking.

#### IV. SEMICLASSICAL QUANTIZATION OF ROTATIONAL CLUSTERS

The RE surface provides the information for determining the appropriate axes for the semiclassical quantization. Since the total angular momentum  $J$  and its projection  $m$  about the lab  $z$  axis are good quantum numbers, it is only necessary to specify one other good quantum number. In this respect, the semiclassical quantization of rotational clusters is a one-dimensional problem for which quantization techniques are highly developed.

As we have seen, in the strict sense, only for the case of a symmetric top is  $k$  the remaining good quantum number. However, the body symmetry axes of the classical trajectories on the asymmetric and octahedral RE surfaces still may be used as axes of semiclassical quantization for the cluster states. For the rigid asymmetric top, the axes of quantization are the body  $\bar{x}$  and  $\bar{z}$  axes as shown in Fig. 4, while for the semirigid spherical top the axes of quantization are the threefold and fourfold symmetry axes as shown in Fig. 5.

To determine the cluster energies or fine structure semiclassically, we use the quantization condition

$$A_n = \int_0^{2\pi} J_\gamma(E_n) d\gamma = 2\pi n, \quad n = J, J-1, \dots, \quad (4.1)$$

where  $J_\gamma$  is the angular momentum about the body axis of quantization. The energy  $E_n$  is varied until the quantization condition is met for a given  $n$ .

The cluster splitting or superfine structure can be determined from the tunneling between equivalent classical trajectories. The tunneling integral is again determined by the topology of the RE surface; the tunneling path is taken on the points between the equivalent trajectories *nearest* the separatrix *with constant energy*. This corresponds to the path of steepest ascent and descent over the saddle point region of the separatrix. Such a path is shown in Fig. 4 by the dashed line through the  $J_\gamma$  axis where the separatrix divides the equivalent trajectories about  $\pm \bar{z}$  for the highest energy cluster of the asymmetric top. For the highest energy cluster of the spherical top, some tunneling paths are shown by the dashed lines in Fig. 5 over the separatrices dividing equivalent trajectories about the  $\pm \bar{x}$ ,  $\pm \bar{y}$ ,  $\pm \bar{z}$  axes.

The superfine tunneling  $S_n$ , between two equivalent trajectories of energy  $E_n$ , is given by

$$S_n = \frac{e^{-|\theta|}}{T}, \quad (4.2)$$

where the period  $T$  of the two equivalent classical trajectories is

$$T = \frac{\partial A_n}{\partial E_n}, \quad (4.3)$$

and the tunneling integral  $\theta$  is given by

$$\theta = i \int_{\text{path}} J_\gamma(E_n) d\gamma. \quad (4.4)$$

The action  $J_\gamma$  is conjugate to the angle  $\gamma$  which now defines the path over the saddle point between the two trajectories. For example, for the path in Fig. 4 between maximal energy trajectories,  $\gamma$  is simply the angle about the  $\bar{x}$  axis, whereas for the path in Fig. 5 on the left,  $\gamma$  is the angle about the  $\bar{z}$  axis.

We shall now give examples of finding the semiclassical cluster energies  $E_n$  and tunneling  $S_n$  for asymmetric top and spherical top molecules. This corresponds to calculating the fine and superfine rotational structure without the need for diagonalizing the Hamiltonian. The accuracy of the semiclassical energies improves with increasing  $J$ .

Our treatment of the asymmetric top using the RE surface is entirely equivalent to that of Colwell, Handy, and Miller,<sup>25</sup> although their emphasis was on low- $J$  levels and ours is on high- $J$  levels for which both treatments are better adapted. To our knowledge, ours is the only complete semiclassical treatment of semirigid spherical top molecules, although approximate semiclassical expressions for the superfine splitting have been given by Watson.<sup>41</sup> Our treatment using the RE surface makes calculating the semiclassical fine and superfine structure for other semirigid molecules straightforward.

### A. Semiclassical treatment of asymmetric top rotors

In order to use Eq. (4.1) to determine the semiclassical cluster energies, we must first determine the angular mo-

mentum  $J_\gamma$  about the  $\bar{z}$  and  $\bar{x}$  axes. First we use the Euler angle coordinates to rewrite the body components of angular momentum

$$J_{\bar{x}} = -J \sin \beta \cos \gamma, \quad (4.5a)$$

$$J_{\bar{y}} = J \sin \beta \sin \gamma, \quad (4.5b)$$

$$J_{\bar{z}} = J \cos \beta \equiv J_\gamma. \quad (4.5c)$$

These relations simply redefine the body polar coordinates ( $-\gamma, -\beta$ ) as explained in Appendix A [see Eq. (A11)]. Substituting these relations into the asymmetric top Hamiltonian Eq. (2.1), one obtains

$$E = A(J^2 - J_\gamma^2) \cos^2 \gamma + B(J^2 - J_\gamma^2) \sin^2 \gamma + CJ_\gamma^2. \quad (4.6)$$

Solving for the  $\gamma$ -conjugate momentum about the  $\bar{z}$  axis yields

$$J_\gamma(\bar{z} \text{ axis}) = \{ [J^2(A \cos^2 \gamma + B \sin^2 \gamma) - E] / [A \cos^2 \gamma + B \sin^2 \gamma - C] \}^{1/2}. \quad (4.7a)$$

By exchanging  $A$  and  $C$  in the above equation, we also determine  $J_\gamma$  about the  $\bar{x}$  axis.

$$J_\gamma(\bar{x} \text{ axis}) = \{ [J^2(C \cos^2 \gamma + B \sin^2 \gamma) - E] / [C \cos^2 \gamma + B \sin^2 \gamma - A] \}^{1/2}. \quad (4.7b)$$

Substituting  $J_\gamma(\bar{z} \text{ axis})$  into Eq. (4.1), we can generate the semiclassical cluster energies about the  $\bar{z}$  axis. These are compared in Table I to the quantum mechanical results of matrix diagonalization for  $J = 10$  and  $J = 20$  using molecular constants  $A = 0.2$ ,  $B = 0.4$ , and  $C = 0.6$  (in  $\text{cm}^{-1}$ ) for a heavy most-asymmetric top molecule. For the special case of the most-asymmetric top, the energies are symmetric about  $BJ(J+1)$  so only the  $\bar{z}$ -axis quantization is necessary. To obtain the most accurate results we let  $J^2 \rightarrow J(J+1)$  for the semiclassical quantizations. Using Eq. (4.3), we may also calculate trajectory periods simultaneously with their quantized energies. These periods are then later used when calculating the tunneling  $S_n$ .

Coincidentally, because of the  $D_{2h}$  symmetry of the RE surface, we may use Eqs. (4.7a) and (4.7b) to calculate the tunneling between the  $\bar{x}$ -axis trajectories and between the  $\bar{z}$ -axis trajectories, respectively. That is, to calculate tunneling between  $\bar{z}$ -axis trajectories in Fig. 4, we use a  $\gamma$  path about the  $\bar{x}$  axis and vice versa. The conjugate momentum  $J_\gamma$  is imaginary on its path over the separatrix saddle points for constant energy  $E_n$  of the cluster. The limits of integration are determined by the condition  $J_\gamma = 0$ . The tunneling  $S_n$  between equivalent trajectories is compared to the quantum mechanical results in Table I.

We have chosen to treat the most-asymmetric top, where the asymmetry parameter  $\kappa = (2B - A - C)/(A - C)$  is zero, in order to test our semiclassical methods. A molecule with  $\kappa = 0$  is farthest from the symmetric top limit  $\kappa = \pm 1$  where  $k = J_z$  is a good quantum number. However, Eqs. (4.7a) and (4.7b) are equally applicable regardless of  $\kappa$  since the positions of the saddle points remain unchanged. That is, the topology of the RE surface is independent of the asymmetry parameter and the axes of quantization remain the same. Only the positions of the contour lines change with  $\kappa$ .

TABLE I. Semiclassical quantization for asymmetric top (in  $\text{cm}^{-1}$ ).

	$E_n(\text{QM})^a$	$E_n(\text{SC})^b$	$S_n(\text{QM})^a$	$S_n(\text{SC})^b$
$n(\bar{z})$			$J = 10$	
10	63.181	63.176	$2.16 \times 10^{-7}$	$1.96 \times 10^{-7}$
9	57.851	57.842	$1.93 \times 10^{-5}$	$1.87 \times 10^{-5}$
8	53.147	53.133	$6.98 \times 10^{-4}$	$6.91 \times 10^{-4}$
7	49.113	49.084	$1.27 \times 10^{-2}$	$1.29 \times 10^{-2}$
6	45.833	45.781	$1.11 \times 10^{-1}$	$1.20 \times 10^{-1}$
$n(\bar{z})$			$J = 20$	
20	246.352	246.347	...	$1.25 \times 10^{-14}$
19	235.360	235.354	$2.84 \times 10^{-12}$	$2.66 \times 10^{-12}$
18	224.977	224.970	$2.55 \times 10^{-10}$	$2.49 \times 10^{-10}$
17	215.214	215.205	$1.42 \times 10^{-8}$	$1.40 \times 10^{-8}$
16	206.083	206.071	$5.33 \times 10^{-7}$	$5.29 \times 10^{-7}$
15	197.603	197.586	$1.41 \times 10^{-5}$	$1.41 \times 10^{-5}$
14	189.801	189.777	$2.71 \times 10^{-4}$	$2.72 \times 10^{-4}$
13	182.721	182.684	$3.76 \times 10^{-3}$	$3.80 \times 10^{-3}$
12	176.448	176.382	$3.64 \times 10^{-2}$	$3.75 \times 10^{-2}$
11	171.132	171.029	$2.18 \times 10^{-1}$	$2.38 \times 10^{-1}$

<sup>a</sup>QM—Quantum mechanical diagonalization.

<sup>b</sup>SC—Semiclassical treatment.

The overall splitting of cluster levels is determined by the number of equivalent trajectories and the possible tunneling for each trajectory. Thus if states  $|1\rangle$  and  $|2\rangle$  correspond to two equivalent trajectories in Fig. 4, we have that  $\langle 1|H|1\rangle = \langle 2|H|2\rangle = E$  and  $\langle 1|H|2\rangle = \langle 2|H|1\rangle = 2S$ . The  $2S$  arises from the fact that there are two equivalent tunneling paths between  $|1\rangle$  and  $|2\rangle$  through the saddle points on the  $\bar{y}$  and  $-\bar{y}$  axes. Thus for these two states, the effective Hamiltonian becomes

$$H = \begin{pmatrix} E & 2S \\ 2S & E \end{pmatrix}. \quad (4.8)$$

Diagonalizing, we find eigenvalues

$$\lambda = E \pm 2S, \quad (4.9)$$

so the overall splitting of the cluster levels is  $4S$ .

The  $J = 20$  extremal cluster in Table I with  $n = 20$  has a tunneling  $2S$  of only  $2.5 \times 10^{-14} \text{ cm}^{-1}$ . This corresponds to the molecule spending 22 min rotating about its  $\bar{z}$  axis before tunneling to the  $-\bar{z}$  axis. Because of symmetry ( $\kappa = 0$ ), the extremal cluster with  $n(x \text{ axis}) = 20$  will have the same tunneling rate. We were unable to calculate the quantum me-

$$J_\gamma^\pm = \left\{ \frac{J^2(\cos^4 \gamma + \sin^4 \gamma) \pm [\epsilon(\cos^4 \gamma + \sin^4 \gamma + 1) - J^4(\cos^4 \gamma + \sin^4 \gamma)]^{1/2}}{\cos^4 \gamma + \sin^4 \gamma + 1} \right\}^{1/2}, \quad (4.13)$$

where

$$\epsilon = (E - BJ^2 + 3J^4/5)/10t_{044}.$$

Equation (4.12b) cannot be solved for  $J_\gamma$  (threefold) in closed form and must be solved numerically. Substituting the values of  $J_\gamma$  into Eq. (4.1), we can calculate the action  $A_n$  and the semiclassical cluster energies  $E_n$ . We use the real solution  $J_\gamma^+$  in Eq. (4.13) for the fourfold cluster energies. The semiclassical energies are compared with the eigenenergies in Table II for  $J = 30$  and  $J = 88$ .<sup>42</sup> We use the known value of

chanical tunneling for this cluster because of the limited precision (16 significant figures) of our computer calculation. For physical processes which occur in time scales less than 22 min, as do hyperfine interactions, the molecule in this cluster state can be treated as rotating about the fixed  $\bar{z}$  symmetry axes with reduced symmetry. As we shall see in Sec. VI, this can lead to the mixing of symmetry species within a cluster due to the hyperfine interaction.

## B. Semiclassical treatment of spherical top rotors

We may use Eq. (4.1) to determine the semiclassical cluster energies for the spherical top rotor by finding the conjugate momentum  $J_\gamma$  about the fourfold and threefold symmetry axes. The spherical top Hamiltonian in Eq. (2.10) is written so that  $J_{\bar{z}}$  is along a fourfold symmetry axis. We may transform to new coordinates:

$$\begin{aligned} J'_x &= (J_{\bar{x}} - J_{\bar{y}})/\sqrt{2}, \\ J'_y &= (J_{\bar{x}} + J_{\bar{y}} - 2J_{\bar{z}})/\sqrt{6}, \\ J'_z &= (J_{\bar{x}} + J_{\bar{y}} + J_{\bar{z}})/\sqrt{3}, \end{aligned} \quad (4.10)$$

such that the new  $J'_z$  lies along the threefold symmetry axis. In terms of these new body angular momenta, the spherical top Hamiltonian becomes (dropping the prime)

$$\begin{aligned} H &= BJ^2 + 10t_{044} [(J_x^4 + J_y^4)/2 + J_z^4/3 + J_x^2 J_y^2 \\ &\quad + 2J_x^2 J_z^2 + 2J_y^2 J_z^2 + 4(3J_x^2 J_y J_z \\ &\quad - J_y^3 J_z)/3\sqrt{2} - 3J^4/5]. \end{aligned} \quad (4.11)$$

Using Eqs. (4.5) to rewrite the body components of angular momentum in terms of Euler angles, the spherical top energy is

$$\begin{aligned} E &= BJ^2 + 10t_{044} [J_\gamma^4(\cos^4 \gamma + \sin^4 \gamma + 1) \\ &\quad - 2J^2 J_\gamma^2(\cos^4 \gamma + \sin^4 \gamma) \\ &\quad + J^4(\cos^4 \gamma + \sin^4 \gamma - 3/5)] \end{aligned} \quad (4.12a)$$

( $J_\gamma$  is about the fourfold symmetry axis)

and

$$\begin{aligned} E &= BJ^2 + 10t_{044} [-7J_\gamma^4/6 + J^2 J_\gamma^2 \\ &\quad + (2\sqrt{2}/3)J_\gamma(J^2 - J_\gamma^2)^{3/2} \sin 3\gamma - J^4/10] \end{aligned} \quad (4.12b)$$

( $J_\gamma$  is about the threefold symmetry axis).

Solving Eq. (4.12a) for  $J_\gamma$  (fourfold), we have

$t_{044} = 5.44 \text{ Hz}$  for  $\text{SF}_6$  which has been determined both from crossover resonances in the  $\text{CO}_2$  saturation spectra of Bordé,<sup>31</sup> and from forbidden transitions in the Doppler-free two-photon spectra of Herlemont.<sup>43</sup> Energies in Table II are given with respect to  $BJ^2$  where  $B = 0.091083 \text{ cm}^{-1}$ .<sup>8</sup>

The quantization occurs for integers  $n_4 = k_4 = J_\gamma J - 1, \dots$  or  $n_3 = k_3 = J_\gamma J - 1, \dots$  until the  $J$  vector crosses a separatrix on the RE surface and is no longer on a trajectory about its axis of quantization for fourfold or threefold clusters, respectively (see Fig. 7). As in the case of

TABLE II. Semiclassical quantization for spherical top ( $\text{cm}^{-1}$ ).

	$E_n(\text{QM})^a$	$E_n(\text{SC})^b$	$S_n(\text{QM})^a$	$S_n(\text{SC})^b$
$J = 30$				
$n_4$				
30	$5.31 \times 10^{-4}$	$5.29 \times 10^{-4}$	$2.63 \times 10^{-11}$	$2.50 \times 10^{-11}$
29	3.54	3.53	$9.55 \times 10^{-10}$	$9.57 \times 10^{-10}$
28	2.04	2.03	$1.53 \times 10^{-8}$	$1.56 \times 10^{-8}$
27	0.80	0.79	$1.42 \times 10^{-7}$	$1.47 \times 10^{-7}$
26	-0.20	-0.22	$8.32 \times 10^{-7}$	$8.65 \times 10^{-7}$
25	-0.97	-1.00	$2.34 \times 10^{-6}$	$3.20 \times 10^{-6}$
$n_3$				
30	$-3.57 \times 10^{-4}$	$-3.54 \times 10^{-4}$	$1.75 \times 10^{-7}$	$1.68 \times 10^{-7}$
29	-2.48	-2.44	$2.02 \times 10^{-6}$	$2.15 \times 10^{-6}$
28	-1.68	-1.66	$6.59 \times 10^{-6}$	$7.40 \times 10^{-6}$
$J = 88$				
$n_4$				
88	$4.206 \times 10^{-2}$	$4.205 \times 10^{-2}$	$1.73 \times 10^{-23}$	$1.62 \times 10^{-23}$
87	3.728	3.727	$2.17 \times 10^{-21}$	$2.13 \times 10^{-21}$
86	3.275	3.273	$1.31 \times 10^{-19}$	$1.30 \times 10^{-19}$
85	2.845	2.844	$5.12 \times 10^{-18}$	$5.11 \times 10^{-18}$
84	2.440	2.438	$1.44 \times 10^{-16}$	$1.44 \times 10^{-16}$
83	2.056	2.055	$3.12 \times 10^{-15}$	$3.13 \times 10^{-15}$
82	1.695	1.694	$5.41 \times 10^{-14}$	$5.44 \times 10^{-14}$
81	1.356	1.355	$7.71 \times 10^{-13}$	$7.77 \times 10^{-13}$
80	1.038	1.037	$9.19 \times 10^{-12}$	$9.28 \times 10^{-12}$
79	0.741	0.739	$9.30 \times 10^{-11}$	$9.40 \times 10^{-11}$
78	0.463	0.462	$8.04 \times 10^{-10}$	$8.15 \times 10^{-10}$
77	0.205	0.204	$5.99 \times 10^{-9}$	$6.09 \times 10^{-9}$
76	-0.033	-0.034	$3.86 \times 10^{-8}$	$3.93 \times 10^{-8}$
75	-0.252	-0.254	$2.15 \times 10^{-7}$	$2.20 \times 10^{-7}$
74	-0.452	-0.454	$1.04 \times 10^{-6}$	$1.06 \times 10^{-6}$
73	-0.633	-0.636	$4.23 \times 10^{-6}$	$4.42 \times 10^{-6}$
72	-0.794	-0.798	$1.44 \times 10^{-5}$	$1.56 \times 10^{-5}$
71	-0.933	-0.939	$4.46 \times 10^{-5}$	$4.54 \times 10^{-5}$
$n_3$				
88	$-2.806 \times 10^{-2}$	$-2.804 \times 10^{-2}$	$1.24 \times 10^{-11}$	$1.17 \times 10^{-11}$
87	-2.493	-2.491	$6.06 \times 10^{-10}$	$5.97 \times 10^{-10}$
86	-2.204	-2.201	$1.37 \times 10^{-8}$	$1.37 \times 10^{-8}$
85	-1.938	-1.935	$1.90 \times 10^{-7}$	$1.94 \times 10^{-7}$
84	-1.697	-1.693	$1.79 \times 10^{-6}$	$1.82 \times 10^{-6}$
83	-1.482	-1.477	$1.17 \times 10^{-5}$	$1.22 \times 10^{-5}$
82	-1.297	-1.290	$5.07 \times 10^{-5}$	$5.63 \times 10^{-5}$
81	-1.146	-1.141	$1.48 \times 10^{-4}$	$1.50 \times 10^{-4}$

<sup>a</sup>QM—Quantum mechanical diagonalization (Ref. 42).

<sup>b</sup>SC—Semiclassical treatment.

the asymmetric top, we let  $J^2 \rightarrow J(J+1)$ . Again, we may simultaneously calculate the period  $T$  for the quantized semiclassical trajectory using Eq. (4.3).

In order to determine the tunneling between two equivalent trajectories for the spherical top rotor, we must first transform  $J_z$  so it is perpendicular to the axes of quantization of the two trajectories such that the conjugate angle  $\gamma$  describes a path over the saddle point on the separatrix between the two trajectories. In the case of tunneling between two fourfold symmetry trajectories,  $J_z$  is transformed by  $90^\circ$  to another fourfold symmetry axis and Eq. (4.12a) may be used again to solve for  $J_\gamma$ . In this case, the solution  $J_\gamma^-$  in Eq. (4.13) is imaginary over the path between equivalent fourfold trajectories and is used in Eq. (4.4) to calculate the tunneling integral  $\theta$ . The limits of integration are determined by the condition  $J_\gamma^- = 0$ .

In the case of tunneling between two threefold symmetry trajectories, we transform  $J_z$  to a perpendicular twofold symmetry axis giving

$$\begin{aligned}
 E = BJ^2 + 10t_{044} [J_x^4/2 + J_y^4 + J_z^4/2 + 3J_x^2J_z^2 \\
 - 3J^4/5] = BJ^2 + 10t_{044} [J_\gamma^4(\cos^4 \gamma \\
 + 2 \sin^4 \gamma - 6 \cos^2 \gamma/2 - J_\gamma^2 J^2(\cos^4 \gamma \\
 + 2 \sin^4 \gamma - 3 \cos^2 \gamma) \\
 + J^4(\cos^4 \gamma + 2 \sin^4 \gamma - 6/5)/2], \quad (4.14)
 \end{aligned}$$

which may be readily solved for  $J_\gamma$  to calculate the tunneling integral  $\theta$ .

As in the case of the asymmetric top, we use the tunneling between equivalent trajectories to calculate the cluster splitting. By diagonalizing the tunneling matrix as was done for Eq. (4.8), we find the following cluster splittings<sup>22-24</sup>:

$$\begin{array}{ll}
 \text{Fourfold splittings} & \text{Threefold splittings} \\
 (A_1 T_1 E): 6S, & (T_2 E T_1): 4S, \\
 (T_2 T_1): 4S, & (A_1 T_1 T_2 A_2): 6S. \\
 (E T_2 A_2): 6S. & 
 \end{array} \quad (4.15)$$

Using these splittings, we compare in Table II the semiclassical tunneling between fourfold and between threefold trajectories with those tunnelings calculated from the matrix diagonalization of Eq. (2.10). The matrix diagonalizations were performed with double precision so that the extremely small splittings could be calculated.<sup>42</sup>

Note that the ratio of superfine splitting to fine structure splitting in the asymmetric top for  $J = 10$  is less than that in the spherical top for  $J = 30$  when comparing extremal clusters energies. The greater tendency for clustering in asymmetric tops than in spherical tops was discussed in the previous section. Also, the extremal fourfold cluster for  $J = 88$  in Table II has a superfine splitting of less than  $2 \times 10^{-23} \text{ cm}^{-1}$  corresponding to less than one tumble in 50 000 yr!

## V. SYMMETRY ANALYSIS OF SPECTRAL CLUSTERS

We review procedures in this section for determining how molecular symmetry species will be grouped into a given set of rotational energy level clusters. The procedures are based upon the theory of coset spaces and induced representations, as was applied to octahedral  $XY_6$  rotational clusters in previous works.<sup>21-24</sup> Here we review and clarify the procedures while applying them to the clusters associated with the molecules  $XY_2$  and  $XY_6$ .

Rotational cluster symmetry analysis is based upon a correlation of symmetry species or irreducible representations of two symmetry groups. One is the symmetry of the RE surface, and the other is the local symmetry of a given classical trajectory. First, let us denote by  $R$  the global rotational symmetry group of an RE surface. For example,  $R = D_2 = \{1, R_{\bar{x}}, R_{\bar{y}}, R_{\bar{z}}\}$  is the rotational symmetry of the asymmetric RE surface shown in Fig. 1(b), where  $R_{\bar{x}}$ ,  $R_{\bar{y}}$ , and  $R_{\bar{z}}$  are  $180^\circ$  rotations around the three principal axes. The characters of  $D_2$  are given in Table III. Secondly, let us denote by  $T$  the local rotational symmetry of a particular classical trajectory. For example, each trajectory which encloses the  $\bar{z}$  axis has a local symmetry  $T = C_2(z) = \{1, R_{\bar{z}}\}$ , i.e., each one is invariant to a  $180^\circ$  rotation around the body  $\bar{z}$  axis.

A classical trajectory symmetry  $T$  must be a proper subgroup of the RE surface symmetry  $R$  (i.e.,  $TCR$ ). Only the separatrix curves [these are represented by dotted (...) lines in Figs. 1 and 2] actually have the full symmetry of the RE surface. However, we noted in Sec. II that a single classical separatrix trajectory is restricted to move only in one direction on a small part of the separatrix in between saddle points. Therefore, individual separatrix trajectories have

even less symmetry than the neighboring trajectories which they separate.

Finally, the correlation between the irreducible representations of  $R$  and  $T$  symmetry determines the allowed cluster structures. It is convenient to express these correlations in table form in which the rows are labeled by the higher  $R$ -symmetry species, and the columns are labeled by the lower  $T$ -symmetry species. For example, the  $T = C_2(z)$  symmetry has odd and even species which are labeled by  $0_2$  and  $1_2$  (zero-mod-two and one-mod-two), respectively, at the head of the columns of the third  $C_2(z)$  correlation table in Fig. 8. Note that the even  $0_2$  column of this table is correlated to the  $(A_1, B_2)$  pair of  $D_2$  species while the odd  $1_2$  column has the  $(A_2, B_1)$  pair. This implies that clusters associated with  $\bar{z}$  rotation will involve  $(A_1, B_2)$  pairs or  $(A_2, B_1)$  pairs for states which are mixtures of  $k$  quanta that are even or odd, respectively. This is what occurs on the right-hand side of the asymmetric top level spectra in Fig. 4. Note that the highest level belongs to an even  $(A_1, B_2)$  cluster since  $J = k = 10$  is an even integer. Similarly, the clusters associated with  $\bar{x}$  rotation will involve  $(A_1, B_1)$  pairs and  $(A_2, B_2)$  pairs for states which are mixtures of  $k$  quanta that are even or odd, respectively, as seen on the left-hand side of Fig. 4.

All three different  $\bar{x}$ ,  $\bar{y}$ , and  $\bar{z}$  rotational  $C_2$  subgroups are correlated with the asymmetric top  $D_2$  symmetry in Fig. 8. Next to each correlation table is a classical sketch of  $XY_2$  rotational motion that would be associated with dynamically broken symmetry or species mixing in each case.

The simplest asymmetric prototypical molecule is the rigid  $XY_2$  complex, and it will be used to demonstrate the symmetry analysis. It should be noted that  $XY_2$  molecular rotational and full point symmetries are  $C_2$  and  $C_{2v}$ , respectively, while its RE surface symmetries are  $D_2$  and  $D_{2h}$ , respectively. The consequences of including full point symmetry will be more fully discussed in the following Sec. VI.

Only two of the three kinds of rotational symmetry breaking actually appear in the rigid asymmetric top spectrum of Fig. 4. The  $C_2(y)$ -type of clusters corresponding to  $(A_1, A_2)$  and  $(B_1, B_2)$  pairs cannot occur as long as the  $\bar{y}$  axis is on a saddle point or anywhere on a separatrix. However, it would be possible for a nonrigid  $XY_2$  molecule to have an RE surface with split separatrices which had orbits around the  $\bar{y}$  axes as well as the  $\bar{x}$  and  $\bar{z}$  axes.

In fact, one cannot rule out the possibility of semirigid asymmetric RE surfaces in which hills or valleys occurred away from symmetry axes or reflection planes as in Fig. 3(a). Then a rotational or rotation-inversion cluster state could involve a mixture of all four  $D_2$  species or even all eight  $D_{2h}$  species. This would be the case if the dynamical symmetry

TABLE III. Characters for  $D_2$  and  $C_{2v}$  symmetry.

$D_2$ :	1	$R_{\bar{x}}$	$R_{\bar{y}}$	$R_{\bar{z}}$
$C_{2v}$ :	1	$IR_{\bar{x}}$	$R_{\bar{y}}$	$IR_{\bar{z}}$
$A_1$	1	1	1	1
$A_2$	1	-1	1	-1
$B_1$	1	1	-1	-1
$B_2$	1	-1	-1	1

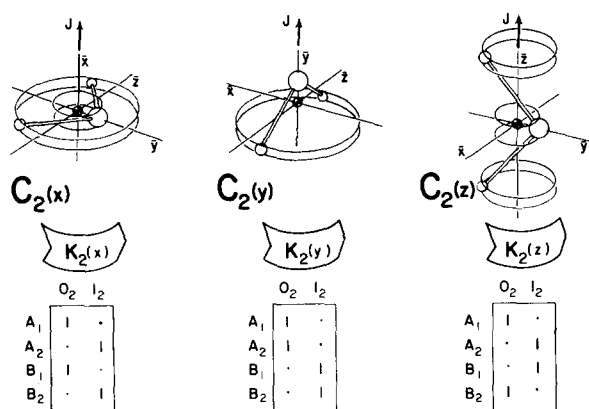


FIG. 8. Symmetry correlations for an asymmetric top with RE surface symmetry  $D_2$  and each of its three twofold subgroups  $C_2(x)$ ,  $C_2(y)$ , and  $C_2(z)$ . The columns of each table give the number of each  $D_2$  species involved in a particular type of cluster after dynamical symmetry breaking. An  $XY_2$  molecular model is shown executing the classical rotation which would correspond to the dynamical symmetry breaking for each case.

broken state corresponds to a classical RE surface trajectory with no symmetry at all.

It is instructive to compare  $D_2$  correlations with symmetry correlations which lead to the predictions of octahedral  $XY_6$  spectral clusters. Three important types of octahedrally ( $R=O$ ) symmetric  $XY_6$  symmetry breaking are represented in Fig. 9, and they are analogous to the corresponding  $XY_2$  symmetry breaking represented in Fig. 8. Again, only the first and third types of symmetry breaking,  $T=C_3$  and  $C_4$ , are applicable to the RE surface trajectories and energy level clusters represented in Fig. 5. The  $XY_6$  separatrix motion associated with the second or  $C_2$ -type of symmetry breaking in Fig. 9 fails to yield clusters just as it did for  $XY_2$  motion. The circulating trajectories on the RE surface in Fig. 5 either have a local symmetry of  $C_3$  or else  $C_4$ . Hamiltonians which lead to  $C_2$  symmetric trajectories include Coriolis effects<sup>36</sup> or higher rank distortion tensors.<sup>44</sup>

The  $XY_6$  spectral clusters in Fig. 5 are labeled by modularity indices  $(0_3, 1_3, 2_3)$  and  $(0_4, 1_4, 2_4, 3_4)$  for clusters associat-

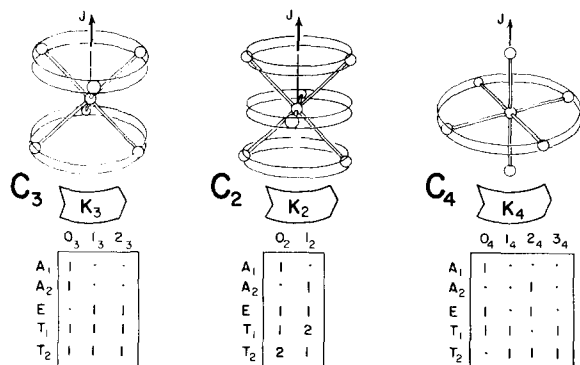


FIG. 9. Symmetry correlations for an octahedral spherical top with RE surface symmetry  $O$  and each of its subgroups  $C_3$ ,  $C_2$ , and  $C_4$ . The columns of each table give the number of each octahedral species involved in a particular type of cluster and dynamical symmetry breaking. An  $XY_6$  molecular model is shown executing the classical rotation which would correspond to the dynamical symmetry breaking for each case.

ed with  $C_3$  and  $C_4$  symmetry, respectively. For example, the lowest threefold or  $C_3$  symmetric trajectory has  $J = k_3 = 30$ , and therefore it belongs to the representations of  $O$  correlated with the zero-mod-three  $O_3$  representation of  $C_3$ , i.e., the first column of the left-hand table in Fig. 9. This corresponds to the  $(A_1, T_1, T_2, A_2)$  cluster on the lower left-hand side of Fig. 5. The fourfold cluster on the right-hand side of the same figure also corresponds to the highest possible  $J = k_4 = 30$  value of angular momentum projection, but it belongs to the  $C_4$  symmetric two-mod-four  $2_4$  cluster. From the third column of the right-hand table in Fig. 9, one obtains the symmetry content of this cluster. This corresponds to the  $(A_2, T_2, E)$  cluster on the lower right-hand side of Fig. 5. The same procedure yields each successive cluster for each  $k_4$  or  $k_3$  value less than  $J = 30$  until the cluster cutoff occurs at the separatrix angle as described previously.

It is appropriate to comment here on the relation between internal or dynamical symmetry breaking which leads to level clustering, and the ordinary external or applied symmetry breaking which leads to level splitting. An example of the latter would be the Zeeman splitting of an atomic  $p$  orbital or octahedral  $T_1$  triplet into three levels of magnetic quanta  $m = 1 \equiv 1_3 \equiv 1_4$ ,  $m = 0 \equiv 0_3 \equiv 0_4$ , and  $m = -1 \equiv 2_3 \equiv 3_4$ , respectively. If the Zeeman  $B$  field were applied along the octahedral  $C_3$  or  $C_4$  axes, the Hamiltonian would be reduced from octahedral  $O$  symmetry to  $C_3$  or  $C_4$  symmetry, respectively. The corresponding level splitting is expressed by the following correlations:  $T_1 \rightarrow 0_3 + 1_3 + 2_3$  of  $C_3$  and  $T_1 \rightarrow 0_4 + 1_4 + 3_4$  of  $C_4$ . These correlations are expressed in the fourth ( $T_1$ ) rows of the  $C_3$  and  $C_4$  tables in Fig. 9.

These examples show that the splitting of orbital degeneracy due to applied symmetry breaking and the clustering due to dynamical or spontaneous symmetry breaking correspond to two sides of the same correlation table. The mathematical explanation of this is based upon the Frobenius reciprocity theorem.<sup>45</sup> The theorem has had a long history of application to problems involving Lorentz groups,<sup>45</sup> crystal space groups,<sup>45,46</sup> symmetry groups of floppy molecules,<sup>47-49</sup> molecular vibrations,<sup>50</sup> and molecular orbitals.<sup>50</sup> The reciprocity theorem and induced representations play a role in the study of vibrational overtones.<sup>51</sup> Clusters corresponding to local modes appear in vibrational overtones of  $XY_6$  spectra, and models have been studied for levels as high as  $20\nu_3$ .<sup>39</sup> Recently, Kellman has applied the reciprocity theorem and related dynamical symmetry breaking theory in a tunneling model of benzene overtones and local modes.<sup>52</sup>

## VI. PERMUTATIONAL SYMMETRY BREAKING AND SUPERHYPERFINE STRUCTURE

About four years ago, the spectroscopy group established by Christian Bordé found the first spectroscopic evidence of strong spin species mixing in  $SF_6$  saturation absorption spectra using ultrastable  $CO_2$  lasers.<sup>31</sup> Their techniques allowed them to detect mixing even in some cases where hyperfine resolution was not achieved. Jacques and Bordé confirmed that species within clusters were mixed by performing detailed numerical diagonalizations of rovibrational-hyperfine tensor Hamiltonians and was able to com-

puter synthesize the laser spectra.<sup>31,32</sup> More recently, the Bordé group<sup>53</sup> has improved their resolution to better than 1.5 kHz and they have found many examples of hyperfine dominated clusters in what has been called *superhyperfine* structure.<sup>54,55</sup> Bordé's conclusions can be summarized by the following excerpt from the introduction to their recent article<sup>32</sup>: "Let us emphasize that, as a consequence of these mixings, superfine and hyperfine structures cannot be treated separately". We show in this section that the importance of superhyperfine structure is not restricted to spherical top molecules but is important to other symmetry types including asymmetric top molecules.

In order to study superhyperfine effects, it is useful to extend the symmetry correlations given in the preceding section to groups which include operations outside of the rotational subgroups. In Sec. II it was noted that an RE surface always has inversion symmetry  $C_i = \{1, I\}$ , where  $I$  represents inversion of points through the origin. Therefore, if the rotational symmetry of the RE surface is  $R$ , then its full rotation-inversion symmetry will be isomorphic to  $R_i = R \times C_i$ . Furthermore, a semirigid molecule has a molecular point symmetry  $S$  which depends on its geometrical and permutational structure, and generally  $S$  is a subgroup of  $R_i$ .

One should be aware that there are several different treatments of rotation-inversion and permutation operations, and that different rules and physical interpretations exist for similar symmetry labels. The most widely used scheme for rovibrational spectroscopy is the permutation inversion (PI) approach which is treated in a review<sup>56</sup> and textbook<sup>57</sup> by Bunker. In discussions of superfine, hyperfine, and dynamical symmetry breaking effects, a modified approach is used which seems to be simpler and more powerful for these purposes. This nonstandard approach was taken independently by Berger<sup>58</sup> and the authors.<sup>24,54,55</sup> Several approaches to symmetry analysis have been compared in a recent monograph by Ezra<sup>59</sup> who preferred the nonstandard approach used here.

The labels of symmetry species in the modified scheme consist of two parts: an external or laboratory part associated with  $O(3)$  (lab) and an internal or molecular structure part associated with  $\bar{O}(3)$  (body). We denote the combined symmetry of the two parts by  $O(3)*\bar{O}(3)$ <sup>60</sup> to indicate the internal and external parts share the same representation label  $J^\rho$ , which consists of total angular momentum and inversion parity ( $J^\rho = 0^+, 0^-, 1^+, 1^-, 2^+, 2^-, \text{etc.}$ ). For a freely rotating semirigid molecule, the external symmetry remains  $O(3)$ . However, for the bent  $XY_2$  molecule the internal point symmetry group is  $S \equiv C_{2v} = \{1, IR_{\bar{x}}, R_{\bar{y}}, IR_{\bar{z}}\}$ , where  $IR_{\bar{x}}$  and  $IR_{\bar{z}}$  are reflections through the  $\bar{y}\bar{z}$  and  $\bar{x}\bar{y}$  planes, respectively as seen in Fig. 8. Thus, the internal part consists of labels  $A_1, A_2, B_1, B_2$  which must be correlated with species  $J^\rho$  of  $\bar{O}(3)$  to determine representations of  $O(3)*C_{2v}$ . This is fundamental to the understanding of the superhyperfine structure of the  $XY_2$  asymmetric top molecule.

The characters of  $C_{2v}$  are given in Table III. Two of the representations, namely  $A_1$  and  $B_1$ , can be related with permutational symmetry and antisymmetry, respectively, according to the sign of  $R_{\bar{y}}$  and  $IR_{\bar{z}}$  operations which permute

the  $Y$  nuclei. Since the  $IR_{\bar{x}}$  reflection in the molecular plane has no effect on the bare  $XY_2$  rotor, only the symmetry species  $A_1$  and  $B_1$  which have unit character for this operation are *allowed*. The  $A_2$  and  $B_2$  species which have ambiguous permutational symmetry are *excluded* as labels of the bare  $XY_2$  rotor.

The permutational symmetry determines which nuclear spin or hyperfine states are associated with species  $A_1$  or  $B_1$ . For Fermi or half-integral-spin  $Y$  nuclei in  $XY_2$ , the total nuclear wave function must be antisymmetric. Then symmetric  $A_1$  species must have antisymmetric or *para* spin functions, while antisymmetric  $B_1$  species must have symmetric or *ortho* spin functions. For Bose or integral-spin nuclei the opposite is true.

Well known Fermi and Bose cases are  $H_2O$  ( $H$  spin = 1/2) and  $D_2O$  ( $D$  spin = 1). *Ortho* and *para* water ( $H_2O$ ) correspond to  $B_1$  and  $A_1$  species with total nuclear spins of  $I = 1$  and  $I = 0$ , respectively. *Para* heavy water ( $D_2O$ ) corresponds to  $B_1$  species with a nuclear spin triplet ( $I = 1$ ) and *ortho* heavy water to species  $A_1$  with a spin sextet ( $I = 0, 2$ ).<sup>24</sup>

For predicting superhyperfine mixing, one must find which combinations of  $O(3)*C_{2v}$  labeled states are allowed in a given cluster. To do this we must compare the characters of symmetry operations of  $C_{2v}$  in the basis  $|J^\rho, k\rangle$  of  $\bar{O}(3)$  with those in Table III. We define the basis of  $\bar{O}(3)$  to be even and odd functions of  $k$ , namely

$$|J^\rho, k^\sigma\rangle = |J^\rho, k\rangle + (-1)^\sigma |J^\rho, -k\rangle. \quad (6.1)$$

These are standing wave states for which the expectation  $\langle J_{\bar{z}} \rangle$  for the rotational angular momentum is zero. In this  $\bar{O}(3)$  basis we have the following characters for  $C_{2v}$  operations using the standard  $D$  matrices and the conventions defined in Appendix A:

$$\langle IR_{\bar{x}} \rangle = \rho \sigma (-1)^J, \quad (6.2a)$$

$$\langle R_{\bar{y}} \rangle = \sigma (-1)^{J+k}, \quad (6.2b)$$

$$\langle IR_{\bar{z}} \rangle = \rho (-1)^k. \quad (6.2c)$$

Comparing to the characters of  $C_{2v}$  in Table III we find the following correlations for clusters about the  $\bar{z}$  axis:

$$\begin{aligned} J \text{ even: } & |A_1, 0_2\rangle \leftrightarrow |J^+, k^+\rangle, \\ & |B_1, 0_2\rangle \leftrightarrow |J^-, k^-\rangle, \\ & |A_1, 1_2\rangle \leftrightarrow |J^-, k^-\rangle, \\ & |B_1, 1_2\rangle \leftrightarrow |J^+, k^+\rangle. \end{aligned} \quad (6.3a)$$

$$\begin{aligned} J \text{ odd: } & |A_1, 0_2\rangle \leftrightarrow |J^+, k^-\rangle, \\ & |B_1, 0_2\rangle \leftrightarrow |J^-, k^+\rangle, \\ & |A_1, 1_2\rangle \leftrightarrow |J^-, k^+\rangle, \\ & |B_1, 1_2\rangle \leftrightarrow |J^+, k^-\rangle. \end{aligned} \quad (6.3b)$$

For clusters about the  $\bar{x}$  axis, we exchange  $\bar{z} \leftrightarrow \bar{x}$  in Table III which corresponds to exchanging species  $B_1 \leftrightarrow B_2$ . This in turn is equivalent to exchanging  $J^\rho \leftrightarrow J^{-\rho}$  in Eqs. (6.3) for correlations to  $B_1$ . Correlations to  $A_1$  remain the same for clusters about the  $\bar{x}$  axis.

Equations (6.3) determine the parity  $\rho$  and the internal  $C_{2v}$  labels of the cluster states for a given  $J$  and  $k$  according to the overall symmetry  $O(3)*C_{2v}$  labels. For the  $XY_2$  example, it is easy to make a connection between the  $O(3)*C_{2v}$  labels

and the standard rotation symmetry labels given previously in Sec. V. For these labels we only considered the "feasible" operations of  $D_2$  which ignore the inversion operation  $I$ . This has the effect for the characters in Table III of multiplying by the inversion species  $A_2$  of  $C_{2v}$  when correlating to  $J^-$  of  $O(3)$ . Thus the labels  $(10^+ * A_1)$  and  $(10^+ * B_1)$  correspond to conventional species  $A_1$  and  $B_1$ , respectively, while the labels  $(10^- * A_1)$  and  $(10^- * B_1)$  correspond to conventional species  $A_2$  and  $B_2$ , respectively. The  $\bar{z}$ -axis cluster sequence implied by Eqs. (6.3) is consistent with the  $D_2$  labeled sequence  $(A_1 B_2)$ ,  $(A_2 B_1)$ ,  $(A_1 B_1)$ , ... obtained on the right-hand side of Fig. 4 using the correlation table in Fig. 8.

The same type of full point symmetry correlations yields the  $O(3) * C_{2v}$  labels of the  $\bar{x}$ -axis cluster sequence. The results for  $J = 10$ , starting with the lowest energy cluster in Fig. 4 are  $\{(10^+ * A_1)(10^+ * B_1)\}$ ,  $\{(10^- * A_1)(10^- * B_1)\}$ ,  $\{(10^+ * A_1)(10^- * B_1)\}$ , ... which is consistent with the  $D_2$  labeled sequence  $(A_1 B_1)$ ,  $(A_2 B_2)$ ,  $(A_1 B_1)$ , ... shown on the left-hand side of Fig. 4.

Importantly, the full  $O(3) * C_{2v}$  symmetry labeling can be used to rule out the possibility for hyperfine mixing in certain types of clusters. For example, all the  $\bar{z}$ -axis clusters for  $XY_2$  contain pairs of states with opposite parity. In the absence of collisions or other external perturbations, the conservation of parity would prohibit the *ortho* and *para* species in  $\bar{z}$ -axis clusters from being perturbed by nuclear spin-rotation interactions.

On the other hand, the  $\bar{x}$ -axis-type clusters contain *ortho* and *para* species with the same overall parity. For these clusters there are no symmetry selection rules which would prohibit hyperfine mixing. The mixing effect of the nuclear spin rotation interaction depends on the detailed rotational and spin dynamics. It is instructive to compare the  $\bar{x}$ -axis rotation depicted in Fig. 8 with the  $\bar{y}$ - and  $\bar{z}$ -axis rotation associated with cluster pairs of opposite parity. If one imagines the nuclei are geometrical points, then an  $\bar{x}$ -axis rotation by  $180^\circ$  is the same as an inversion. This is not the case for the  $\bar{y}$  or  $\bar{z}$  axis rotational motion. The classical  $\bar{y}$  or  $\bar{z}$  axis rotational motion [or, equivalently, moving wave quantum states with nonzero expectation values  $\langle J_{\bar{y}} \rangle = k_2(y)$  or  $\langle J_{\bar{z}} \rangle = k_2(z)$ ] must involve mixed inversion parity, and thus the  $\bar{y}$ - and  $\bar{z}$ -type clusters contain species of opposite parity. Only the  $\bar{y}$ - and  $\bar{z}$ -type standing wave states [such as Eq. (6.1)] have definite + or - inversion parity and each corresponds to a different *ortho* or *para* species.

One should notice that the  $\bar{z}$ -type rotational motion shown in Fig. 8 puts the identical  $Y$  nuclei in nonoverlapping orbits, i.e., they tend to be permutationally isolated. This by itself is enough to guarantee that the permutational symmetry species are mixed. However, as we noted, it also involves mixing parity so that parity conserving perturbations such as hyperfine interactions cannot cause such mixing by themselves. On the other hand, all of the  $XY_6$  motions in Fig. 9 correspond to permutational isolation which can be accomplished with or without parity mixing, and therefore all these clusters *must* undergo hyperfine mixing when the superfine splitting is less than the hyperfine splitting. For the  $\bar{x}$ -type  $XY_2$  clusters, hyperfine mixing is not forbidden by parity conservation, but neither is it required by permutational

considerations since the  $Y$  nuclei may move in overlapping orbits as shown in Fig. 8.

We now consider some more extreme forms of rotational symmetry breaking and hyperfine mixing than those which occur in the  $\bar{x}$ -axis cluster examples just treated. Extreme forms of symmetry breaking occur when the classical trajectories put equivalent nuclei into orbits which are physically very different or which isolate the nuclei into permutational subsets which do not overlap appreciably. This might happen to an  $XY_2$  molecule, e.g., if it fell into a rotational state associated with the classical motion depicted in Fig. 3. The quantum state corresponding to this motion would be a combination of the four clustered species  $(A_1 B_1 A_2 B_2)$ , i.e., the states occurring in the correlation of  $D_2$  with the trivial  $C_1$  symmetry. (A standing wave version of this state which had definite parity would be a combination of the *ortho* and *para* pair  $A_1$  and  $B_1$  or else the pair  $A_2$  and  $B_2$ .)

Part of the symmetry breaking is connected with the difference in physical environments which the two identical nuclei find themselves in Fig. 3(b). One nucleus finds itself close to the rotational axis and revolving in the lab around a smaller circle [circle 1 in Fig. 3(b)] than the other nucleus [circle 2 in Fig. 3(b) is the larger one]. Presumably, the nucleus in state 1 would experience a different magnetic field than the one in state 2.

Another part of the symmetry breaking is connected with the permutational isolation or reduced overlap between the identical particles. If the superfine splittings are negligible, then the molecule cannot tunnel or tumble into one of the other equivalent dynamical configurations which might allow the  $Y$  nuclei to overlap and trade positions in the laboratory.

Of course, one can never know which of the two  $Y$  nuclei is in rotational state 1 or state 2 since they carry no permanent markings that distinguish them. However, if the  $Y$  nuclei have a nonzero intrinsic spin, then this may serve as a temporary marking device. For spin-1/2 nuclei, it is relatively easy to see how such a marking can lead to a mixing of *para*  $A_1$  and *ortho*  $B_1$  species.

Consider the  $m_I = 0$  states of the *para* and *ortho* species. The *para* state has a symmetrized  $A_1$  spatial part  $|\boxed{12}\rangle$  with an antisymmetrized spin part  $|\boxed{\uparrow\downarrow}\rangle$ , which is a zero total spin  $I = 0$  singlet. The *ortho* state has an antisymmetrized  $B_1$  spatial part  $|\boxed{21}\rangle$  with a symmetrized spin part  $|\boxed{\uparrow\uparrow}\rangle$  which is part of a unit total spin  $I = 1$  triplet. These may be related to Slater determinant states in which the spin up or down serves as a marker. One such state is the following:

$$|\boxed{1\uparrow}\rangle = \left\{ \left| A_1 \boxed{12\uparrow} \right\rangle - \left| B_1 \boxed{21\uparrow\downarrow} \right\rangle \right\} / \sqrt{2}, \quad (6.4)$$

in which the nucleus in state 1 has spin up while the one in state 2 has spin down. This is likely to have a different energy than the reverse state

$$|\boxed{1\downarrow}\rangle = \left\{ \left| A_1 \boxed{12\uparrow} \right\rangle + \left| B_1 \boxed{21\uparrow\downarrow} \right\rangle \right\} / \sqrt{2}, \quad (6.5)$$

since the magnetic environment for state 1 is likely to differ from that of state 2. If the difference is large compared to the superfine splitting of  $A_1$  and  $B_1$  species, then the eigenstates

will be  $(A_1, B_1)$  mixtures similar to Eqs. (6.4) and (6.5).

Some conditions for superhyperfine mixing which are sufficient but not necessary have been described above. A complete description of mixing conditions is obviously beyond the scope of this paper. For each class of RE surface trajectories (this classification presents a formidable task in itself), one must consider the effects of all possible spin-rotation and spin-spin interactions for a given polyatomic molecule. This needs to be accompanied by spectroscopy that is as detailed and comprehensive as that which was done for  $SF_6$  and related molecules.

However, at least two necessary conditions for collision-free or spontaneous species mixing have emerged. One is that at least two species in a cluster must have the same parity. Parity was shown to be a key consideration in  $SF_6$  superhyperfine spectroscopy.<sup>31,32,54,55</sup> The other condition is that superfine or cluster splitting be comparable to or smaller than the hyperfine splitting.

## VII. CONCLUSIONS AND FUTURE WORK

We have shown how RE surfaces can be used to understand the complex rotational fine, superfine, and superhyperfine structure of semirigid polyatomic rotors. We have focused attention on the energy levels of rotations and vibration-rotations that can adequately be described by a single isolated RE surface, and we have discussed the most elementary form of semiclassical eigenvalue calculations for asymmetric and octahedrally symmetric rotors. We have made analogies between the RE surface as it applies to rotational levels and the well-known concept of the PE surface which applies to vibrational levels.

Analogies between RE and PE surfaces continue to be valuable as we contemplate future work. More advanced semiclassical theory is leading to methods for deriving eigenfunctions, transition rates, and detailed intra- and intermolecular dynamics as well as more accurate eigenvalues. We are encouraged by the success of Heller, Davis, and De Leon<sup>61</sup> in finding eigenfunctions and transitions on anharmonic PE surfaces using wave packet or coherent state propagation. Blanco and Heller have also begun to consider simple rovibrational models using a combination of rotational projection and wave packet propagation.<sup>62</sup> It should be possible to extend these methods to the domain of RE surfaces so that a more detailed description of rovibronic dynamics can be made.

The detailed dynamics of even the simplest rotor models still hold some unanswered questions. One question involves various forms of rotational relaxation or angular momentum delocalization. We have discussed the precession and tunneling processes in Sec. III B, and related them to fine and superfine structure, respectively. However, there is another form of delocalization which will occur even at high  $J$  and far from any separatrices. This has to do with the second energy derivative of the action, i.e., with the gradual change in intercluster spacing or fine structure with energy. Uneven fine structure should be associated with a gradual dephasing and spreading of an angular momentum wave packet or quasicohherent state. Only quantum systems with exactly equally spaced energy levels can be expected to be

have coherently forever, like a harmonic oscillator. This lack of coherence applies even to the simplest rigid symmetric rotor [recall Fig. 1(a)] since its Hamiltonian varies quadratically with angular momentum. The spreading, as well as possible reemergence of rotational wave packets, needs to be understood.

The problems associated with multiple RE surfaces are being explored. The crossing or near avoided crossing of two or more RE surfaces would lead to resonance effects analogous to the Jahn-Teller-Renner effects associated with the crossing of two PE surfaces. Such crossings of RE surfaces would provide a detailed semiclassical framework for visualizing complex rovibrational or rovibronic interactions. Development of multiple RE surface representations should be useful for studying molecules which are floppy or highly excited. Also, an analogy with the Franck-Condon principle for PE surfaces can be made for transitions between RE surfaces as well.

A general introduction to the effects of spectral clustering should probably mention something about collisions, since, for one thing, they were mentioned in the introductory quote by Herzberg.<sup>29</sup> Since the concept of rotational species needs to be modified in the presence of clusters, it is likely that detailed properties and selection rules for collisions or reactions would be affected as well. Curl, Kasper, and Pitzer<sup>63</sup> considered spin species conversion through "accidental" degeneracies in an early paper on spin state equilibrium and nonmagnetic collisions. However, they did not have knowledge of either the extent or the details of rotational superfine structure. Now that this is coming available, it should be possible to make more precise predictions using their theory. It should also be possible to modify spin species selection rules developed by Quack<sup>64</sup> for chemically reactive scattering. So far, dynamical symmetric breaking effects have not been considered in these rules.

In summary, there is considerable evidence for unexpected structural details in rotational, rovibrational, and rovibronic spectra of polyatomic molecules. The potential applications and fundamental importance of these details makes it worthwhile to build a theoretical framework with which to understand them.

## ACKNOWLEDGMENT

One of us (WGH) would like to thank the National Science Foundation for support from Grant PHY-8207150 for theoretical physics.

## APPENDIX A

### 1. Angular coordinates for RE surface analysis

We shall try to present a physically intuitive review of the coordinates and momenta for rotational dynamics in general and RE surface theory in particular. To facilitate this approach we shall reintroduce a mechanical analog device shown in Fig. 10 for elucidating Euler angles.<sup>24,65</sup> The device serves to define Euler angles in a nonabstract way and show that they are natural choices.

The Euler device (Fig. 10) consists of four frames: a lab of  $(x)$  frame, an  $(x')$  frame, an  $(x'')$  frame, and a body or  $(\bar{x})$

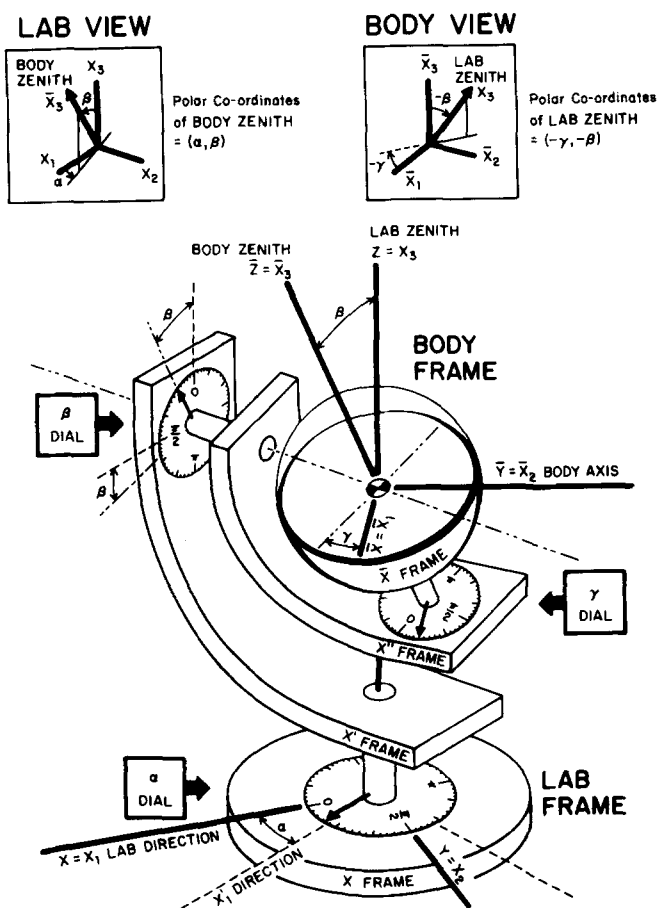


FIG. 10. Mechanical definition of Euler coordinates for RE surface mechanics. Laboratory and body views of the body and lab zeniths are shown in respective insets. The RE surface coordinates are based on the body view.

## 2. Rotation transformation between lab and body

The vector rotation transformation between frames is very well known, and rederivation is given here solely to maintain the continuity of development based on Fig. 10. A lab rotation operator  $R(\alpha, \beta, \gamma)$  may be defined using an *ordered* set of *lab based* operations which set the Euler dials from  $(0, 0, 0)$  to  $(\alpha, \beta, \gamma)$ . Ordering becomes important for noncommuting fixed base operations.  $R(\alpha \beta \gamma)$  equals a product of a  $\gamma$  rotation around the lab  $z = x_3$  axis, followed by a  $\beta$  rotation around by  $y = x_2$  axis, followed by an  $\alpha$  rotation around the  $z = x_3$  axis as shown in Fig. 11.

The matrix representation of this product is

$$\langle R(\alpha \beta \gamma) \rangle = \begin{pmatrix} \cos \alpha & -\sin \alpha & 0 \\ \sin \alpha & \cos \alpha & 0 \\ 0 & 0 & 1 \end{pmatrix} \begin{pmatrix} \cos \beta & 0 & \sin \beta \\ 0 & 1 & 0 \\ -\sin \beta & 0 & \cos \beta \end{pmatrix} \begin{pmatrix} \cos \gamma & -\sin \gamma & 0 \\ \sin \gamma & \cos \gamma & 0 \\ 0 & 0 & 1 \end{pmatrix} \quad (A1)$$

$$= \begin{matrix} \mathbf{x}_1 \\ \mathbf{x}_2 \\ \mathbf{x}_3 \end{matrix} \begin{pmatrix} \cos \alpha \cos \beta \cos \gamma - \sin \alpha \sin \gamma & -\cos \alpha \cos \beta \sin \gamma - \sin \alpha \cos \gamma & \cos \alpha \sin \beta \\ \sin \alpha \cos \beta \cos \gamma + \cos \alpha \sin \gamma & -\sin \alpha \cos \beta \sin \gamma + \cos \alpha \cos \gamma & \sin \alpha \sin \beta \\ -\sin \beta \cos \gamma & \sin \beta \sin \gamma & \cos \beta \end{pmatrix} \begin{matrix} \bar{\mathbf{x}}_1 \\ \bar{\mathbf{x}}_2 \\ \bar{\mathbf{x}}_3 \end{matrix}$$

## 3. Angular velocities and momenta for RE surface analysis

The kinematics of a rotating frame may also be described by successive combination of three simple rotations. The time derivative of any vector ( $\mathbf{r}$ ) in the lab  $x$  frame can be written in terms of a time derivative viewed in the  $x'$  frame as follows:

frame, with each of the first three frames connected to the next one in the sequence by one of three pivots. Each of the three pivots have an angular dial which displays one of the Euler angles  $\alpha$ ,  $\beta$ , or  $\gamma$ . Euler angles so defined are clearly holonomic (i.e., integrable) coordinates whose values depend only on orientations of the four frames relative to chosen dial zero points and not on the path or order of operations which led to an orientation.

The choice of dial zero points is based upon conventions for labeling axes and is of one of the sources of confusion about Euler angles. The choice is made in Fig. 10 so that the pair  $(\alpha, \beta)$  are polar coordinates (i.e., azimuth and polar angle, respectively) of the body zenith ( $\bar{z} = \bar{x}_3$  axis) in the lab frame, and the pair  $(-\gamma, -\beta)$  are polar coordinates of the lab zenith ( $z = x_3$  axis) in the body frame. The insets in Fig. 10 show the lab and body views separately. (Note that an azimuth angle is a longitude measured counterclockwise from an  $x$  axis. The complement of a latitude is a polar angle measured from the  $z$  axis.)

In the case of classical free rotation, one may choose the lab-fixed angular momentum vector  $\mathbf{J}$  to be fixed along the lab  $z = x_3$  axis. Then the coordinate pair  $(-\gamma, -\beta)$  will be the azimuth and polar angles, respectively, for points on an RE surface. The angular momentum trajectory in  $(-\gamma, -\beta)$  space will be along an RE surface topography line as previously explained. For this choice of  $\mathbf{J}$ , the effect of  $\alpha$ -angle rotation does not manifest itself on the classical trajectory in body  $(-\gamma, -\beta)$  space since then  $\alpha$  is just the "twist" of the  $z$  axis as it moves along an RE topography line. For other choices of  $\mathbf{J}$  in the lab, the  $z$ -axis trajectory in body  $(-\gamma, -\beta)$  space will be a quasicycloidal nutation around the precession path of an RE topography line.

$$\left. \frac{d\mathbf{r}}{dt} \right|_x = \left. \frac{d\mathbf{r}}{dt} \right|_{x'} + \boldsymbol{\omega}_\alpha \times \mathbf{r},$$

where

$$\begin{aligned} \boldsymbol{\omega}_\alpha &= \dot{\alpha} \mathbf{x}_3 \\ &= \dot{\alpha} (-\sin \beta \cos \gamma \bar{\mathbf{x}}_1 + \sin \beta \sin \gamma \bar{\mathbf{x}}_2 \\ &\quad + \cos \beta \bar{\mathbf{x}}_3) \end{aligned} \quad (A2)$$

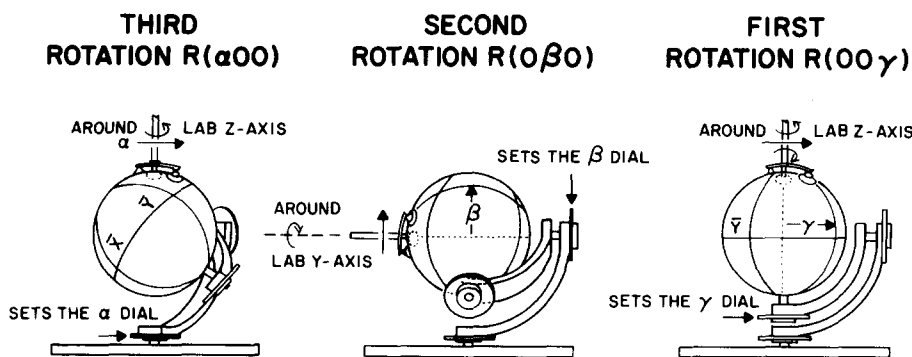


FIG. 11. Operational definition of Euler coordinates. Ordered rotational sequence  $R(\alpha 0 0)R(0 \beta 0)R(0 0 \gamma) = R(\alpha \beta \gamma)$  of lab-based operations orients the body into the  $(\alpha \beta \gamma)$  position relative to the lab. Only rotations about the lab  $y$  and  $z$  axes are used.

is the  $\alpha$ -dial angular velocity vector. [Equation (A2) is used to get the body representation.] A similar relation for the  $x'$ -frame derivative in terms of the  $x''$ -frame derivative is

$$\frac{d\mathbf{r}}{dt}\Big|_{x'} = \frac{d\mathbf{r}}{dt}\Big|_{x''} + \boldsymbol{\omega}_\beta \times \mathbf{r},$$

where

$$\boldsymbol{\omega}_\beta = \dot{\beta}(-\sin \alpha \mathbf{x}_1 + \cos \alpha \mathbf{x}_2) = \dot{\beta}(\sin \gamma \bar{\mathbf{x}}_1 + \cos \gamma \bar{\mathbf{x}}_2) \quad (\text{A3})$$

is the  $\beta$  angular velocity as seen by examining Fig. 10. Finally, the  $x''$ -frame derivative can be written in terms of the body  $\bar{x}$ -frame derivative

$$\frac{d\mathbf{r}}{dt}\Big|_{x''} = \frac{d\mathbf{r}}{dt}\Big|_{\bar{x}} + \boldsymbol{\omega}_\gamma \times \mathbf{r},$$

where

$$\boldsymbol{\omega}_\gamma = \dot{\gamma}(\cos \alpha \sin \beta \mathbf{x}_1 + \sin \alpha \sin \beta \mathbf{x}_2 + \cos \beta \mathbf{x}_3) = \dot{\gamma} \bar{\mathbf{x}}_3 \quad (\text{A4})$$

is the  $\gamma$  angular velocity.

Combining Eqs. (A2)–(A4) gives the total angular velocity  $\boldsymbol{\omega}$  of the body  $\bar{x}$ -frame relative to the lab  $x$  frame, i.e.,

$$\frac{d\mathbf{r}}{dt}\Big|_x = \frac{d\mathbf{r}}{dt}\Big|_{\bar{x}} + \boldsymbol{\omega} \times \mathbf{r}, \quad (\text{A5a})$$

where

$$\boldsymbol{\omega} = \boldsymbol{\omega}_\alpha + \boldsymbol{\omega}_\beta + \boldsymbol{\omega}_\gamma. \quad (\text{A5b})$$

This yields the following relations between the Euler angular velocities and the lab components of  $\boldsymbol{\omega}$ :

$$\begin{pmatrix} \omega_x \\ \omega_y \\ \omega_z \end{pmatrix} = \begin{pmatrix} 0 & -\sin \alpha & \cos \alpha \sin \beta \\ 0 & \cos \alpha & \sin \alpha \sin \beta \\ 1 & 0 & \cos \beta \end{pmatrix} \begin{pmatrix} \dot{\alpha} \\ \dot{\beta} \\ \dot{\gamma} \end{pmatrix}, \quad (\text{A6a})$$

$$\begin{pmatrix} \dot{\alpha} \\ \dot{\beta} \\ \dot{\gamma} \end{pmatrix} = \begin{pmatrix} -\cos \alpha \cot \beta & -\sin \alpha \cot \beta & 1 \\ -\sin \alpha & \cos \alpha & 0 \\ \frac{\cos \alpha}{\sin \beta} & \frac{\sin \alpha}{\sin \beta} & 0 \end{pmatrix} \begin{pmatrix} \omega_x \\ \omega_y \\ \omega_z \end{pmatrix}. \quad (\text{A6b})$$

The same relations for the body components are as follows:

$$\begin{pmatrix} \omega_{\bar{x}} \\ \omega_{\bar{y}} \\ \omega_{\bar{z}} \end{pmatrix} = \begin{pmatrix} -\sin \beta \cos \gamma & \sin \gamma & 0 \\ \sin \beta \sin \gamma & \cos \gamma & 0 \\ \cos \beta & 0 & 1 \end{pmatrix} \begin{pmatrix} \dot{\alpha} \\ \dot{\beta} \\ \dot{\gamma} \end{pmatrix} \quad (\text{A6c})$$

$$\begin{pmatrix} \dot{\alpha} \\ \dot{\beta} \\ \dot{\gamma} \end{pmatrix} = \begin{pmatrix} -\frac{\cos \gamma}{\sin \beta} & \frac{\sin \gamma}{\sin \beta} & 0 \\ \sin \gamma & \cos \gamma & 0 \\ \cot \beta \cos \gamma & -\cot \beta \sin \gamma & 1 \end{pmatrix} \begin{pmatrix} \omega_{\bar{x}} \\ \omega_{\bar{y}} \\ \omega_{\bar{z}} \end{pmatrix}. \quad (\text{A6d})$$

These relations allow one to relate the canonical lab based angular momenta

$$J_x = \frac{\partial H}{\partial \omega_x}, \quad J_y = \frac{\partial H}{\partial \omega_y}, \quad J_z = \frac{\partial H}{\partial \omega_z} \quad (\text{A7})$$

and the body based angular momenta

$$J_{\bar{x}} = \frac{\partial H}{\partial \omega_{\bar{x}}}, \quad J_{\bar{y}} = \frac{\partial H}{\partial \omega_{\bar{y}}}, \quad J_{\bar{z}} = \frac{\partial H}{\partial \omega_{\bar{z}}} \quad (\text{A8})$$

to the Euler canonical momenta.

$$J_\alpha = \frac{\partial H}{\partial \dot{\alpha}}, \quad J_\beta = \frac{\partial H}{\partial \dot{\beta}}, \quad J_\gamma = \frac{\partial H}{\partial \dot{\gamma}}. \quad (\text{A9})$$

Applying the chain rule and Eq. (A6b) one derives the lab based momenta

$$\begin{pmatrix} J_x \\ J_y \\ J_z \end{pmatrix} = \begin{pmatrix} -\cos \alpha \cot \beta & -\sin \alpha & \frac{\cos \alpha}{\sin \beta} \\ -\sin \alpha \cot \beta & \cos \alpha & \frac{\sin \alpha}{\sin \beta} \\ 1 & 0 & 0 \end{pmatrix} \begin{pmatrix} J_\alpha \\ J_\beta \\ J_\gamma \end{pmatrix}. \quad (\text{A10})$$

Similarly, using Eq. (A6d) one obtains body based momenta

$$\begin{pmatrix} J_{\bar{x}} \\ J_{\bar{y}} \\ J_{\bar{z}} \end{pmatrix} = \begin{pmatrix} -\frac{\cos \gamma}{\sin \beta} & \sin \gamma & \cot \beta \cos \gamma \\ \frac{\sin \gamma}{\sin \beta} & \cos \gamma & -\cot \beta \sin \gamma \\ 0 & 0 & 1 \end{pmatrix} \begin{pmatrix} J_\alpha \\ J_\beta \\ J_\gamma \end{pmatrix}. \quad (\text{A11})$$

The same relations apply to the quantum angular momentum operators. The Euler momentum operators may be represented by partial derivatives with respect to Euler angles.

$$J_\alpha = (\hbar/i) \frac{\partial}{\partial \alpha}, \quad J_\beta = (\hbar/i) \frac{\partial}{\partial \beta}, \quad J_\gamma = (\hbar/i) \frac{\partial}{\partial \gamma}. \quad (\text{A12})$$

Such simple representations of the lab or body momentum

operators are not as useful since the angular coordinates conjugate to  $J_x$ ,  $J_y$ , or  $J_z$  are not holonomically defined.

Nevertheless, by using Eqs. (A10) and (A11), one verifies that the lab operators satisfy standard commutation relations

$$[J_x, J_y] = ih J_z \text{ (and cyclically)}, \quad (\text{A13})$$

while the body operators satisfy reversed relations<sup>24,33</sup>:

$$[J_{\bar{x}}, J_{\bar{y}}] = -ih J_{\bar{z}} \text{ (and cyclically)}. \quad (\text{A14})$$

The two sets are mutually commuting,<sup>35,36</sup> i.e.,

$$[J_{\bar{x}}, J_y] \equiv 0, \text{ etc.} \quad (\text{A15})$$

It is easy to see that the Euler momenta [Eq. (A12)] are commutative, i.e.,

$$[J_\alpha, J_\beta] \equiv 0, \text{ etc.} \quad (\text{A16})$$

This is consistent with the independence of the three dials in Fig. 10.

- <sup>1</sup>J. P. Aldridge, H. Filip, H. Flicker, R. F. Holland, R. S. McDowell, N. G. Nereson, and K. Fox, *J. Mol. Spectrosc.* **58**, 165 (1975).  
<sup>2</sup>R. S. McDowell, H. W. Galbraith, C. D. Cantrell, N. G. Nereson, and E. D. Hinkley, *J. Mol. Spectrosc.* **68**, 288 (1977).  
<sup>3</sup>Ch. J. Bordé, M. Ouhayoun, A. Van Lerberghe, C. Saloman, S. Avriplier, C. D. Cantrell, and J. Bordé, *Laser Spectroscopy IV*, edited by H. Walther and K. W. Rothe (Springer, New York, 1979).  
<sup>4</sup>K. C. Kim, W. B. Person, D. Seitz, and B. J. Krohn, *J. Mol. Spectrosc.* **76**, 322 (1979).  
<sup>5</sup>P. F. Moulton, D. M. Larsen, J. N. Walpole, and A. Mooradian, *Opt. Lett.* **1**, 51 (1977).  
<sup>6</sup>C. W. Patterson, R. S. McDowell, P. F. Moulton, and A. Mooradian, *Opt. Lett.* **6**, 93 (1981).  
<sup>7</sup>A. S. Pine and A. G. Robiette, *J. Mol. Spectrosc.* **80**, 388 (1980).  
<sup>8</sup>C. W. Patterson, B. J. Krohn, and A. S. Pine, *J. Mol. Spectrosc.* **88**, 133 (1981).  
<sup>9</sup>C. Reiser, J. I. Steinfeld, and H. W. Galbraith, *J. Chem. Phys.* **74**, 2189 (1981).  
<sup>10</sup>M. Dubs, D. Harradine, E. Schweitzer, and J. I. Steinfeld, and C. W. Patterson, *J. Chem. Phys.* **77**, 3824 (1982).  
<sup>11</sup>F. Herlemont, M. Lyszyk, and J. Lemaire, *Appl. Phys.* **24**, 3691 (1981).  
<sup>12</sup>R. S. McDowell, C. W. Patterson, N. G. Nereson, F. R. Petersen, and J. S. Wells, *Opt. Lett.* **6**, 422 (1981).  
<sup>13</sup>C. W. Patterson, R. S. McDowell, N. G. Nereson, B. J. Krohn, J. S. Wells, and F. R. Petersen, *J. Mol. Spectrosc.* **91**, 416 (1982).  
<sup>14</sup>C. W. Patterson and A. S. Pine, *J. Mol. Spectrosc.* **96**, 404 (1982).  
<sup>15</sup>M. Takami and H. Kuze, *J. Chem. Phys.* **78**, 2204 (1983).  
<sup>16</sup>R. S. McDowell, M. J. Reinfeld, H. W. Galbraith, B. J. Krohn, H. Flicker, R. C. Kennedy, J. P. Aldridge, and N. G. Nereson, *J. Mol. Spectrosc.* **83**, 440 (1980).  
<sup>17</sup>M. Takami, *J. Chem. Phys.* **73**, 2665 (1980); **72**, 4276 (1981); **76**, 1670 (1982).  
<sup>18</sup>G. A. Laguna, K. C. Kim, C. W. Patterson, M. J. Reinfeld, and D. M. Seitz, *Chem. Phys. Lett.* **75**, 357 (1980).  
<sup>19</sup>K. Fox, H. W. Galbraith, B. J. Krohn, and J. D. Louck, *Phys. Rev. A* **15**, 1363 (1977).  
<sup>20</sup>A. J. Dorney and J. K. G. Watson, *J. Mol. Spectrosc.* **42**, 135 (1972).  
<sup>21</sup>W. G. Harter and C. W. Patterson, *Phys. Rev. Lett.* **38**, 224 (1977).  
<sup>22</sup>W. G. Harter and C. W. Patterson, *J. Chem. Phys.* **66**, 4872 (1977).  
<sup>23</sup>C. W. Patterson and W. G. Harter, *J. Chem. Phys.* **66**, 4886 (1977).  
<sup>24</sup>W. G. Harter, C. W. Patterson, and F. J. da Paixao, *Rev. Mod. Phys.* **50**, 37 (1978).  
<sup>25</sup>S. M. Colwell, N. C. Handy, and W. H. Miller, *J. Chem. Phys.* **68**, 745 (1978).  
<sup>26</sup>G. W. King, *J. Chem. Phys.* **15**, 820 (1947).  
<sup>27</sup>R. M. Hainer, P. C. Cross, and G. W. King, *J. Chem. Phys.* **17**, 826 (1949).

- <sup>28</sup>M. Born, *The Mechanics of the Atom*, translated by J. W. Fisher and D. R. Hartree (Fredrick Ungar, New York, 1927), p. 99.  
<sup>29</sup>G. Herzberg, *Infrared and Raman Spectra* (Van Nostrand, New York, 1945), p. 468.  
<sup>30</sup>W. G. Harter and C. W. Patterson, in *Advances in Laser Chemistry*, edited by A. H. Zewail (Springer, New York, 1978), p. 455.  
<sup>31</sup>J. Bordé, Ch. J. Bordé, C. Saloman, A. Van Lerberghe, M. Ouhayoun, and C. D. Cantrell, *Phys. Rev. Lett.* **45**, 14 (1980).  
<sup>32</sup>J. Bordé and Ch. J. Bordé, *Chem. Phys.* **71**, 417 (1982).  
<sup>33</sup>L. D. Landau and E. M. Lifshitz, *Mechanics*, translated by J. B. Sykes and J. S. Bell (Addison-Wesley, Reading, MA., 1966).  
<sup>34</sup>W. G. Harter, *Am. J. Phys.* **44**, 1080 (1976).  
<sup>35</sup>A. Bohr and B. R. Mottelson, *Nuclear Structure* (Academic, New York, 1978), Vol. II, p. 184.  
<sup>36</sup>W. G. Harter, C. W. Patterson, and H. W. Galbraith, *J. Chem. Phys.* **69**, 4896 (1978).  
<sup>37</sup>H. W. Galbraith, C. W. Patterson, B. J. Krohn, and W. G. Harter, *J. Mol. Spectrosc.* **73**, 475 (1978).  
<sup>38</sup>C. W. Patterson, H. W. Galbraith, B. J. Krohn, and W. G. Harter, *J. Mol. Spectrosc.* **77**, 457 (1979).  
<sup>39</sup>R. S. McDowell, C. W. Patterson, and W. G. Harter, *Los Alamos Sci.* **3**, 38 (1982).  
<sup>40</sup>The cone nomogram fits rovibrational spectra as well as the energy levels since the RE surfaces for the ground and vibrational excited states have the same shape.  
<sup>41</sup>J. K. G. Watson, Thirty-Second Symposium on Molecular Spectroscopy, Ohio State University, 1977.  
<sup>42</sup>B. J. Krohn, Los Alamos Report LA-6554-MS, 1976.  
<sup>43</sup>C. W. Patterson, F. Herlemont, M. Lyszyk, and J. Lemaire, *J. Mol. Spectrosc.* (submitted).  
<sup>44</sup>W. G. Harter and C. W. Patterson, *J. Math. Phys.* **20**, 1453 (1979).  
<sup>45</sup>J. S. Lomont, *Applications of Finite Groups* (Academic, New York, 1959), pp. 202, 226, 315.  
<sup>46</sup>S. L. Altman, *Induced Representations in Crystals and Molecules* (Academic, New York, 1977).  
<sup>47</sup>H. C. Longuet-Higgins, *Mol. Phys.* **6**, 445 (1963).  
<sup>48</sup>J. K. G. Watson, *Can. J. Phys.* **43**, 1996 (1965).  
<sup>49</sup>B. J. Dalton, *J. Chem. Phys.* **54**, 4745 (1971); B. J. Dalton and P. D. Nicholson, *Int. J. Quantum Chem.* **9**, 325 (1975).  
<sup>50</sup>W. G. Fately, et al., *Infrared and Raman Selection Rules: The Correlation Method* (Wiley-Interscience, New York, 1972).  
<sup>51</sup>H. W. Galbraith and C. D. Cantrell, in *The Significance of Nonlinearity in the Natural Sciences, Studies in the Natural Sciences*, edited by A. Perlmutter and L. F. Scott (Plenum, New York, 1977), Vol. 13, p. 227.  
<sup>52</sup>M. E. Kellman, *J. Phys. Chem.* **87**, 2161 (1981).  
<sup>53</sup>J. Borde, Thirty-Eighth Symposium on Molecular Spectroscopy, Ohio State University, 1983.  
<sup>54</sup>W. G. Harter and C. W. Patterson, *Phys. Rev. A* **10**, 2277 (1979).  
<sup>55</sup>W. G. Harter, *Phys. Rev. A* **24**, 192 (1981).  
<sup>56</sup>P. R. Bunker, *Vibrational Spectroscopy and Structure*, edited by J. R. Durig (Marcel Dekker, New York, 1975), Vol. 3.  
<sup>57</sup>P. R. Bunker, *Molecular Symmetry and Spectroscopy* (Academic, New York, 1979).  
<sup>58</sup>H. Berger, *J. Phys. (Paris)* **38**, 1371 (1977).  
<sup>59</sup>G. S. Ezra, *Symmetry Properties of Molecules: Lecture Notes in Chemistry* (Springer, New York, 1982), Vol. 28, p. 41.  
<sup>60</sup>J. D. Louck and H. W. Galbraith, *Rev. Mod. Phys.* **48**, 69 (1976). The notation  $O(3)_{\text{lab}} * S(\text{body})$  used in this reference implies a cross product ( $\times$ ) of mutually commuting  $O(3)$  group or subgroup representations which are correlated to the same angular momentum and parity.  
<sup>61</sup>M. J. Davis and E. J. Heller, *J. Chem. Phys.* **75**, 3916 (1981); N. De Leon and E. J. Heller, *ibid.* **78**, 4005 (1983).  
<sup>62</sup>M. Blanco and E. J. Heller, *J. Chem. Phys.* **78**, 2504 (1983).  
<sup>63</sup>R. F. Curl, J. V. V. Kaspar, and K. S. Pitzer, *J. Chem. Phys.* **46**, 3220 (1967).  
<sup>64</sup>M. Quack, *Mol. Phys.* **34**, 447 (1977).  
<sup>65</sup>Such a device was built by W. Harter, W. Lees, and P. Wollerman at the Joint Institute of Laboratory Astrophysics and by W. Harter and K. Springfield at the Georgia Institute of Technology. A detailed description of these devices and a related analog device is available through EARTHINGS Co., Cleveland, Ohio 44017.